Advanced piezoelectric fluid energy harvesters by monolithic fluid-structure-piezoelectric coupling: a full-scale finite element model

Runze Zhang, Yu Cong, Mohammed Sellam, Amer Chpoun, Shuitao Gu

Advanced piezoelectric fluid energy harvesters by monolithic fluid-structure-piezoelectric coupling: a full-scale finite element model

R. Z. Zhang [a], **Y. Cong** [a], **M. Sellam** [a], **A. Chpoun** [a]. **S. T. Gu** [b].

[a] *Université Paris-Saclay, Univ Evry, LMEE, 91020, Evry, France*

[b] *School of Civil Engineering, Chongqing University, Chongqing 400044, China*

Abstract

A full-scale finite element model is presented for monolithic fluid-structure interaction (FSI) simulations of thin-walled piezoelectric fluid energy harvesters (PFEH). Unlike widely used beam/plate-based models, our model employs a solid finite element discretization to precise represent the complex PFEH designs involving microstructured transducers and non-uniform cantilevers. These features, plus the local FSI effects, are often ignored by simplified models. We applied the Galerkin method to formulate the weak form of the mixed equation system, integrating the flow dynamics, the geometrically nonlinear cantilever, the piezoelectric components, the electrode, and the output circuit within a closed-circuit electro-mechanical coupled system. The coupling of the multiple domains is achieved through boundary-fitted discretization within a monolithic scheme, using shifted-Crank–Nicolson temporal integration. This work explored implementing piezoelectric FSI systems within the FEniCS-based TurtleFSI library, and experimented techniques such as employing penalty functions for achieving electrode components with uniform electric potentials. We investigated various advanced PFEH features, including the base plate design, the arrangement and microstructure of the piezoelectric components, and their influence on the system's dynamic and energy output behavior. The results confirmed the model's effectiveness and potential to assist the design and optimization of PFEH systems.

Keywords: Fluid-structure interaction; Monolithic coupling; Thin-walled piezoelectric energy harvester; Geometric nonlinearity.

1 Introduction

In the domains of the Internet of Things (IoT) [1] and renewable energy [2], piezoelectric fluid energy harvesters (PFEH) [3, 4, 5] are increasingly recognized as viable alternatives to conventional batteries for powering low-power electronic devices [6]. These devices offer substantial application value and development potential due to their ability to harness complex fluid-structure interactions (FSI) [7].

Corresponding authors:
runze.zhang@univ-evry.fr (R. Z. Zhang). gust@cqu.edu.cn (S. T. Gu).

Such interactions initiate vibrations in the base plate, subsequently causing piezoelectric patches to deform and generate electrical energy through the direct piezoelectric effect [8, 9]. The efficiency of PFEH systems greatly depends on the design of the base plate and piezoelectric patches, particularly their shape and microstructure. Therefore, high-fidelity numerical simulations that enable full-scale modeling of PFEH components and their interaction with fluid dynamics are essential for optimizing the design of these advanced systems.

Simulating PFEH systems presents significant challenges, particularly in accurately predicting fluid dynamic loads. This process necessitates the simultaneous consideration of structural deformation and its resultant feedback on the fluid field [10]. Currently, coupling methods for fluid-structure interaction (FSI) are primarily categorized into monolithic [11] and partitioned methods [12]. Partitioned methods handle different physical fields separately, transferring data between them via an FSI interface using interpolation algorithms [13]. This approach benefits from software modularity, allowing independent numerical schemes for each subsystem [14]. The growing cost-effectiveness of numerical simulations has recently popularized partitioned methods for FSI [15]. These methods are further divided into strong and weak coupling types [16]; strong coupling is achieved by incorporating iterative algorithms at the FSI interface, enhancing equilibrium conditions at each timestep.

Monolithic methods solve nonlinear equations in both the fluid and solid domains simultaneously, effectively meeting strong coupling and boundary equilibrium conditions. Known for their robustness and stability [17], these methods are particularly apt for scenarios where solid and fluid densities are similar, leading to strong coupling effects, such as in blood flow within vessels [11, 18] and vibrations of slender, thin-walled structures in dense liquids [19]. However, monolithic methods require substantial computational resources, which may limit their suitability for large-scale applications. Additionally, matching interfaces in fluid-structure coupling is critical. The Arbitrary Lagrangian-Eulerian (ALE) method [20] and the Immersed Boundary Method (IBM) [21] are two prominent approaches for managing interface boundaries in complex flows. ALE, a boundary-fitted method, is straightforward to implement and effective for high Reynolds number scenarios, enabling precise tracking of moving FSI interfaces. However, it may struggle with large structural torsions or translations and complex fluid domain topologies. Conversely, IBM excels in handling intricate geometrical structures and significant deformations without necessitating fluid mesh movement, although it can be challenging to precisely define coupling interfaces, potentially reducing accuracy in strong FSI scenarios. When computational resources allow, it is advantageous to integrate a monolithic coupling algorithm with a boundary-fitted approach like ALE to enhance the accuracy of simulation results [22].

In the simulation of piezoelectric fluid energy harvesters (PFEH), adopting a continuum model for solid modeling is crucial to effectively design the shape, internal structure, and layout of the base plate and piezoelectric patch. Recent research on fluid-structure-piezoelectric coupling simulation methods often employs non-volumetric models such as beam [22, 23, 24] or shell models [25]. These models facilitate the modeling of thin structures with fewer mesh elements, significantly reducing computational time. However, they may introduce discontinuities in the pressure field at the moving FSI interface, adding complexity to simulations. Techniques like the level-set method [20] and fluid domain splitting method [22] have been developed to address these challenges. Nonetheless, non-volumetric finite elements struggle to accurately represent the influence of the solid's geometry and internal structure on the flow field, and the reciprocal effects of these interactions. As interest grows in the composite structure design [26] of energy harvesters and the microstructure design of piezoelectric patches [27, 28], the use

of solid continuum models becomes increasingly vital. While recent advancements in the monolithic simulation of PFEH using solid continuum models have typically focused on small deformations [29], the unique thin-walled and slender characteristics of PFEH demand the consideration of geometric nonlinearities. This would more accurately capture the nonlinear vibrational behaviors observed in dynamic flow fields [30] and simplify the representation of anisotropic materials. A comprehensive numerical method that incorporates geometric nonlinearity within solid modeling remains an area ripe for further exploration. Such an approach promises to enhance the reliability and efficiency of PFEH structures, optimizing their energy harvesting capabilities.

In this context, we propose a comprehensive fluid-structure-piezoelectric coupling algorithm within the FEniCS finite element solution framework [31]. This algorithm is designed to simultaneously address structural deformation, fluid flow, and electrical output. We employ a solid continuum model for structural modeling that incorporates geometric nonlinearities. The piezoelectric material is described using a constitutive model that extends the solid equations to include the influence of external circuits. To ensure uniform potential across the electrode surfaces, a penalty function method is utilized. The fluid dynamics are modeled using the Navier-Stokes (NS) equations, integrated with the ALE method to accurately represent the FSI boundary. Fluid mesh motions are managed through a biharmonic model to maintain mesh quality during deformation. The governing equations for these physical fields are combined into a unified system, discretized spatially and temporally using the Galerkin finite element method and a shifted Crank-Nicolson scheme. Solutions are computed at each time step through Newton iteration, ensuring accuracy and stability across the simulation. To demonstrate the necessity and effectiveness of employing a solid model, we have developed a series of test cases. These cases vary the shapes, positions, and internal structures of the base plate and piezoelectric patch, illustrating the method's potential to significantly enhance the design and performance of PFEH systems. This approach not only highlights the capabilities of our modeling strategy but also underscores its application value across diverse PFEH configurations.

This paper is structured to systematically present the theory, numerical implementation, validations, and the results achieved using the proposed monolithic coupling method. Section 2 delineates the governing equations for all fields involved in PFEH, emphasizing the modeling of the solid domain as a volumetric continuum. Section 3 introduces the monolithic solution scheme for the coupled system, detailing the techniques used for modeling the electrodes and output circuits within the piezoelectric solid domain. Section 4 validates this coupling scheme by comparing it with a FSI benchmark case that includes geometric nonlinearities and a piezoelectric structure case using output circuits from commercial software. In Section 5, the methodology is applied to study a thin-walled PFEH positioned behind a rigid cylinder within a fluid flow environment. This section discusses the effects of varying base plate sections and designs of the piezoelectric patch through two groups of numerical cases. Finally, Section 6 discusses the contributions and limitations of the current work, providing a critical assessment of the approach and suggesting avenues for future research.

2 Governing equations of fluid-structure-piezoelectric coupled system

In this section, we outline the basic notations used in the equations of the coupled system, which involves the fluid dynamics (presented in both Euler and ALE-transformed coordinate systems), the structure kinematics (covering both pure elastic and piezoelectric solid materials in the Lagrangian coordinates), and the coupling conditions that integrate these domains.

2.1 Basic notations

This study explores the conversion of ambient flow kinetic energy into electrical energy through the flow-induced vibrations of piezoelectric patches mounted to a cantilevered base structure. Initially, the fluid's energy is transformed into cyclic strain within the piezoelectric material, which, due to the piezoelectric effect, generates electrical energy that an external circuit then captures. This process can be illustrated by the model shown in Figure 1, depicting a classic unimorph piezoelectric energy harvester (PEH) driven by fluid flows. The PEH configuration includes an elastic base plate mounted on a rigid cylinder, a piezoelectric patch covered by electrodes on both its upper and lower surfaces, and an electrical circuit composed of a simple resistor element. As fluid flows past the host cylinder, vortex shedding initiates flow-induced vibrations in the base plate, which in turn causes the piezoelectric materials to deform. The domain of this integrated fluid-structure-piezoelectric interaction problem, denoted by $\Omega \subset \mathbb{R}^2$, is analyzed over the time interval T.

The domain Ω is assumed to be time-independent and comprises three time-dependent subdomains in its current configuration: $\Omega_f(t)$ for the fluid domain, $\Omega_{ss}(t)$ for the elastic solid domain, and $\Omega_{sp}(t)$ for the piezoelectric solid domain. The structural components of the energy harvester, involving the elastic and piezoelectric solids, interact with the fluid flow via the fluid-structure interface, denoted by $\Gamma_{\text{FSI}}(t) = \partial\Omega_f(t) \cap \partial\Omega_s(t)$, where $\partial\Omega_s = \partial\Omega_{ss} \cup \partial\Omega_{sp}$ represents the combined boundary of the structural domains. The initial configuration of these domains, or their configuration at any subsequent reference point in time, is represented by $\widehat{\Omega}_f$, $\widehat{\Omega}_{ss}$, and $\widehat{\Omega}_{sp}$, with their interface denoted as $\widehat{\Gamma}_{\text{FSI}}$. The external boundary of the entire domain is given by $\partial\widehat{\Omega} = \widehat{\Gamma} = \widehat{\Gamma}_{\text{D}} \cup \widehat{\Gamma}_{\text{N}}$, where $\widehat{\Gamma}_{\text{D}}$ and $\widehat{\Gamma}_{\text{N}}$ correspond to the Dirichlet and Neumann boundaries, respectively. In the following sections, we will detail the field equations and coupling conditions that govern the dynamics of this multiphysics system.

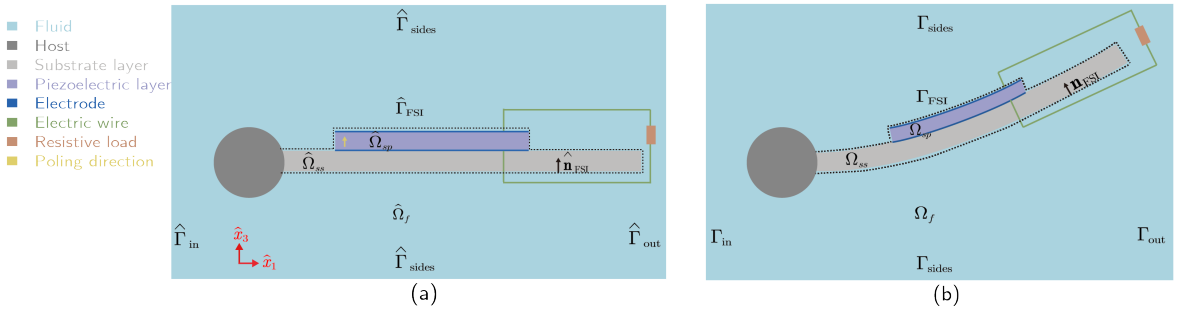

Figure 1: A unimorph flow-driven PEH: in its reference configuration (a), and the current configuration (b).

2.2 Equations of fluid dynamics

In solving fluid flow problems on fixed meshes, the Eulerian description is frequently used for reasons of practicality, especially in handling large fluid distortions. However, this description becomes challenging when it comes to accurately tracking moving interfaces involving different media due to its fixed observation point. An alternative, the Lagrangian description, overcomes this by moving the fluid mesh nodes with the material particles, making it adept at tracking the interfaces between different media, but struggles with the treatment of large distortions of complex vortex structures. To bridge the gap between these two approaches, we adopt the Arbitrary Lagrangian-Eulerian (ALE) reference configuration. This intermediate framework expresses the fluid equations in artificial coordinates, offering an effective way to model fluid-structure interactions. In the following, we begin the detailed discussion with the Eulerian Navier-Stokes equations and then extend to the ALE formulation of these equations.

Navier-Stokes equations in the Eulerian framework:

The dynamics of an incompressible, viscous fluid is most intuitively described using Eulerian coordinates, for which the observer focuses on specific points in the space through which fluid particles flow over time. In this framework, the spatial domain occupied by the fluid at any given moment is denoted by Ω_f. The velocity and pressure fields within this domain are represented by $\mathbf{v}_f(\mathbf{x}, t)$ and $p_f(\mathbf{x}, t)$, respectively, where $\mathbf{x}$ indicates a point within the fluid's current domain, as illustrated in Figure 1 (b). We utilize the Navier-Stokes equations to describe the fluid motion, which gives

$$\rho_f \left.\frac{\partial \mathbf{v}_f}{\partial t}\right|_{\mathrm{x}} + \rho_f \mathbf{v}_f \cdot \nabla \mathbf{v}_f = \nabla \cdot \boldsymbol{\sigma}_f, \qquad \text{in } \Omega_f,\, t \in T, \tag{1}$$

$$\nabla \cdot \mathbf{v}_f = 0, \qquad \text{in } \Omega_f,\, t \in T, \tag{2}$$

where ρ_f denotes the fluid density. For enhanced clarity, Eq. (1) and Eq. (2) describe the momentum and mass conversation in the context of incompressible, viscous Newtonian fluids. Within Eq. (1), the left-hand side comprises both the time derivative and the convection terms. On the other hand, the right-hand side involves the divergence of the fluid stress tensor, which characterizes the internal forces arising from viscosity and pressure. The constitutive relation for a Newtonian fluid, which defines the stress tensor, is expressed as follows:

$$\boldsymbol{\sigma}_f = \boldsymbol{\sigma}_{fp} + \boldsymbol{\sigma}_{fv} = -p\mathbf{I} + 2\mu_f \boldsymbol{\varepsilon}_f. \tag{3}$$

This equation implies that the total internal stress tensor $\boldsymbol{\sigma}_f$ in a homogeneous fluid comprises the isotropic pressure component $\boldsymbol{\sigma}_{fp}$ and the viscous shear stress tensor $\boldsymbol{\sigma}_{fv}$. In this relation, $\mathbf{I}$ is the identity matrix, signifying that the pressure acts equally in all directions, and μ_f is the fluid's dynamic viscosity, a measure of its resistance to flow. The rate-of-strain tensor $\boldsymbol{\varepsilon}_f$, capturing the deformation rates within the fluid, is derived from the fluid's velocity field as:

$$\boldsymbol{\varepsilon}_f = \frac{1}{2}\left(\nabla \mathbf{v}_f + (\nabla \mathbf{v}_f)^{\mathrm{T}}\right). \tag{4}$$

Here, the operator $\nabla = \partial/\partial \mathbf{x}$ indicates spatial derivatives with respect to the position vector $\mathbf{x}$, placing the observer in the context of the Eulerian description within the dynamic fluid domain Ω_f. To fully define the fluid's behavior, Eq. (1) and (2) are accompanied by appropriate boundary conditions.

Among these, the velocity is prescribed on the Dirichlet boundary $\Gamma_{f,D}$ within the fluid domain Ω_f:

$$\mathbf{v}_f = \mathbf{g}_f \ , \quad \text{on} \ \ \Gamma_{f,D} \subset \partial\Omega_f. \tag{5}$$

The imposed velocity is defined by the function $\mathbf{g}_f : \Gamma_{f,D} \times T \to \mathbb{R}^2$. This type of Dirichlet condition is typically applied at the inflow velocity boundary and at the boundaries where the no-slip condition is assumed, such as solid walls in contact with the fluid. For the external stresses acting on the fluid, Neumann boundary conditions are introduced as follows:

$$\boldsymbol{\sigma}_f \cdot \mathbf{n}_f = \mathbf{h}_f, \quad \text{on} \ \ \Gamma_{f,N} \subset \partial\Omega_f, \tag{6}$$

where $\Gamma_{f,N}$ represents the Neumann boundaries within the fluid domain Ω_f, $\mathbf{h}_f$ denotes the prescribed stress vector, and $\mathbf{n}_f$ is the outward normal vector at the fluid boundary. The Neumann boundary condition is commonly applied at the outflow boundary. It is often referred to as a "do-nothing" condition, implying the condition of natural flow exit or of constant pressure, allowing the fluid to exit the domain without additionally imposed stresses.

Navier-Stokes equations in ALE framework:

Applying the Navier-Stokes equations (Eqs. (1) and (2)) directly in the context of FSI problems, such as for PEH modeling, poses significant challenges due to the evolving fluid and solid domains. Unlike traditional fluid dynamics simulations where the fluid domain Ω_f is static, using fixed points $\mathbf{x}$ to observe fluid variables $\mathbf{v}_f$ and p_f, modeling PEHs with FSI requires considering a fluid domain that moves with the solid domain. As a modeling strategy, we choose to consider fixed $\mathbf{x}$ in regions distant from the fluid-structure boundary, unaffected by its movement. Then, for the regions under the influence of fluid-structure interactions, we employ the Arbitrary Lagrangian Eulerian (ALE) approach to model the fluid-structure dynamics. Within this framework, an auxiliary displacement field, denoted as $\widehat{\mathbf{u}}_\mathrm{A}$, is introduced to facilitate the transition of the fluid equations between the current and the reference configurations:

$$\widehat{\mathbf{u}}_\mathrm{A}(\widehat{\mathbf{x}}, t) = \mathbf{x} - \widehat{\mathbf{x}} = \widehat{\mathcal{A}}(\widehat{\mathbf{x}}, t) - \widehat{\mathbf{x}} \quad \text{for} \quad \widehat{\mathbf{x}} \in \widehat{\Omega}_f. \tag{7}$$

In this equation, we use the operator $\widehat{\mathcal{A}}$ to map the current position of the fluid domain Ω_f relative to its reference state $\widehat{\Omega}_f$. Unlike the solid domain's displacement field, the auxiliary displacement field $\widehat{\mathbf{u}}_\mathrm{A}$ is determined without solving the fluid dynamics equations. Further details on this will be presented in section 2.3.

In the ALE formulation of the Navier-Stokes equations for the moving fluid domain Ω_f, it is important to relate the material time derivative $\frac{\mathrm{d}\mathbf{v}_f}{\mathrm{d}t}$ to the partial time derivative $\left.\frac{\partial \mathbf{v}_f}{\partial t}\right|_{\mathbf{x}}$ within an Eulerian framework. This relationship is expressed as: $\frac{\mathrm{d}\mathbf{v}_f}{\mathrm{d}t} = \left.\frac{\partial \mathbf{v}_f}{\partial t}\right|_{\mathbf{x}} + \mathbf{v}_f \cdot (\nabla \mathbf{v}_f)$, which combines the local temporal changes and the convective transport effects of the fluid flow. Extending this concept to the ALE framework, we define an ALE time derivative, $\left.\frac{\partial \mathbf{v}_f}{\partial t}\right|_{\widehat{\mathbf{x}}}$, incorporating the mesh's movement into the fluid's velocity field:

$$\left.\frac{\partial \mathbf{v}_f}{\partial t}\right|_{\widehat{\mathbf{x}}} = \left.\frac{\partial \mathbf{v}_f}{\partial t}\right|_{\mathbf{x}} + \mathbf{v}_\mathrm{A} \cdot (\nabla \mathbf{v}_f) \tag{8}$$

where $\mathbf{v}_\mathrm{A}$ refers to the Lagrangian velocity associated with the mesh motion in the fluid domain Ω_f. It is generally different from $\mathbf{v}_f$ which reflects the fluid's physical velocity, and is related to the auxiliary

displacement field by:

$$\mathbf{v}_{\mathrm{A}} = \left.\frac{\partial \widehat{\mathcal{A}}}{\partial t}\right|_{\widehat{\boldsymbol{x}}} \circ \widehat{\mathcal{A}}^{-1} \,, \tag{9}$$

where $\widehat{\mathcal{A}}^{-1}$ allows mapping the deformation velocity of Ω_f from the reference configuration to the current configuration. Integrating Eqs. (8,9) into the Navier-Stokes equations (Eqs. (1,2)), we arrive at the modified momentum conservation in the moving fluid domain Ω_f:

$$\rho_f \left.\frac{\partial \mathbf{v}_f}{\partial t}\right|_{\widehat{\mathbf{x}}} + \rho_f \left(\mathbf{v}_f - \mathbf{v}_{\mathrm{A}}\right) \cdot \nabla \mathbf{v}_f = \nabla \cdot \boldsymbol{\sigma}_f, \quad \text{in } \Omega_f, \tag{10}$$

along with the incompressibility condition:

$$\nabla \cdot \mathbf{v}_f = 0, \qquad \text{in } \Omega_f, \tag{11}$$

Comparing with the standard momentum conservation described in Eq. (1), an additional convective term related to the mesh motion, and as a function of $\mathbf{v}_{\mathrm{A}}$, emerges in Eq. (10). The value of $\mathbf{v}_{\mathrm{A}}$ varies depending on the chosen framework for the motion description. In a Eulerian framework, $\mathbf{v}_{\mathrm{A}} = 0$. Then in a Lagrangian description, $\mathbf{v}_{\mathrm{A}}$ equals the physical fluid velocity $\mathbf{v}_f$: the mesh moves synchronously with the fluid. The ALE framework allows a flexible transition between these Eulerian and Lagrangian descriptions. The mesh motion may either track the fluid, remain fixed, or be set arbitrarily between these two states. While the ALE approach effectively incorporates fluid mesh motion, it describes the fluid dynamics within the current configuration of Ω_f. This description complicates the integration with structural equations, which are typically defined relative to a reference configuration. In this context, $\widehat{\Omega}_f$ signifies the spatial fluid domain in its reference state. In the reference configuration, the fluid velocity $\widehat{\mathbf{v}}_f$ at the position $\widehat{\mathbf{x}}$ corresponds to the Eulerian fluid velocity $\mathbf{v}_f$ at the current position $\mathbf{x}$, and similarly for the pressure fields. We now proceed to adapt these equations to the fixed, stress-free reference region as illustrated in Figure 1 (a):

$$\rho_f \widehat{\boldsymbol{J}}_{\mathrm{A}} \left.\frac{\partial \widehat{\mathbf{v}}_f}{\partial t}\right|_{\widehat{\mathbf{x}}} + \rho_f \widehat{\boldsymbol{J}}_{\mathrm{A}} \widehat{\mathbf{F}}_{\mathrm{A}}^{-1} \left(\widehat{\mathbf{v}}_f - \widehat{\mathbf{v}}_{\mathrm{A}}\right) \cdot \widehat{\nabla} \widehat{\mathbf{v}}_f = \widehat{\nabla} \cdot \left(\widehat{\boldsymbol{J}}_{\mathrm{A}} \widehat{\boldsymbol{\sigma}}_f \widehat{\mathbf{F}}_{\mathrm{A}}^{-\mathbf{T}}\right), \quad \text{in } \widehat{\Omega}_f, \tag{12}$$

$$\widehat{\nabla} \cdot \left(\widehat{\boldsymbol{J}}_{\mathrm{A}} \widehat{\mathbf{F}}_{\mathrm{A}}^{-1} \widehat{\mathbf{v}}_f\right) = 0, \qquad \text{in } \widehat{\Omega}_f, \tag{13}$$

where the deformation gradient $\widehat{\mathbf{F}}_{\mathrm{A}}$ is defined as $\widehat{\nabla} \widehat{\mathbf{u}}_{\mathrm{A}} + \mathbf{I}$, and $\widehat{\boldsymbol{J}}_{\mathrm{A}} = \det(\widehat{\mathbf{F}}_{\mathrm{A}})$ is its determinant.The differentiation operator $\widehat{\nabla} = \partial / \partial \widehat{\mathbf{x}}$ refers here to the derivatives with respect to the spatial position $\widehat{\mathbf{x}}$. In the reference configuration, the fluid mesh motion is described by the velocity given by:

$$\widehat{\mathbf{v}}_{\mathrm{A}} = \left.\frac{\partial \widehat{\mathcal{A}}}{\partial t}\right|_{\widehat{\boldsymbol{x}}} = \frac{\partial \left(\widehat{\mathbf{u}}_{\mathrm{A}} + \widehat{\mathbf{x}}\right)}{\partial t} = \frac{\partial \widehat{\mathbf{u}}_{\mathrm{A}}}{\partial t}. \tag{14}$$

Since $\widehat{\boldsymbol{x}}$ is the fixed position on the fluid reference configuration, independent of time t, then the transformed fluid stress tensor is given by:

$$\widehat{\boldsymbol{\sigma}}_f = \widehat{\boldsymbol{\sigma}}_{fp} + \widehat{\boldsymbol{\sigma}}_{fv} = -\widehat{p}_f \mathbf{I} + \rho_f \mu_f \left(\left(\nabla \widehat{\mathbf{v}}_f\right) \widehat{\mathbf{F}}_{\mathrm{A}}^{-1} + \widehat{\mathbf{F}}_{\mathrm{A}}^{-\mathrm{T}} \left(\nabla \widehat{\mathbf{v}}_f\right)^{\mathrm{T}}\right) . \tag{15}$$

The governing equations Eq. (14) and (15) should be complemented by boundary conditions, analogous

to those detailed in Eq. (5) and (6), as

$$\widehat{\mathbf{v}}_f = \widehat{\mathbf{g}}_f \ , \quad \text{on } \ \widehat{\Gamma}_{f,D} \subset \partial\widehat{\Omega}_f, \tag{16}$$

$$\left(\boldsymbol{J}_{\mathrm{A}}\widehat{\boldsymbol{\sigma}}_f\mathbf{F}_{\mathrm{A}}^{-\mathbf{T}}\right)\cdot\widehat{\mathbf{n}}_f = \widehat{\mathbf{h}}_f, \quad \text{on } \ \widehat{\Gamma}_{f,N} \subset \partial\widehat{\Omega}_f \tag{17}$$

where $\widehat{\Gamma}_{f,D}$ and $\widehat{\Gamma}_{f,N}$ denote the Dirichlet and Neumann boundaries of the reference fluid domain $\widehat{\Omega}_f$, respectively. The normal vector on these boundaries, $\widehat{\mathbf{n}}_f$, is oriented outward from $\widehat{\Omega}_f$ towards adjacent subdomains.

2.3 Fluid mesh motion using a biharmonic model

Accurately modeling the fluid mesh movement is important for FSI problems within the ALE framework. This requires properly defining the deformation of the fluid mesh in response to the structural boundary motion that interacts with the fluid media. To address this, the auxiliary displacement field $\widehat{\mathbf{u}}_{\mathrm{A}}$, introduced earlier in Section 2.2, is utilized to extend the structural deformations into the fluid domain. The auxiliary displacement field represents the motion of the fluid mesh without incorporating inertial effects. In this study, the biharmonic equation [32] is employed to govern the mesh movement. This choice is informed by comparative studies with other mesh movement models, such as harmonic [33, 34] and linear-elastic [35, 36] models. The biharmonic model provides greater flexibility in accommodating diverse boundary and interface conditions, ensuring that the fluid mesh deforms smoothly in sync with large structural deformations [37, 38]. In the reference configuration, $\widehat{\Omega}_f$, this model is uses an intermediate variable $\widehat{\boldsymbol{\eta}}_{\mathrm{A}}$, defined as follows:

$$\widehat{\boldsymbol{\eta}}_{\mathrm{A}} = -\alpha_u\widehat{\Delta}\widehat{\mathbf{u}}_{\mathrm{A}}, \quad -\alpha_u\widehat{\Delta}\widehat{\boldsymbol{\eta}}_{\mathrm{A}} = 0, \quad \text{in } \widehat{\Omega}_f, \tag{18}$$

where α_u is an artificial material parameter, typically determined empirically, that regulates the mesh motion. Following the recommendations from [38], it is convenient to adopt a small positive value for α_u, which leads to optimal performance. Additionally, the mesh model requires the implementation of suitable boundary conditions. To obtain clearer expressions, we express the auxiliary displacement field $\widehat{\mathbf{u}}_{\mathrm{A}}$ and the intermediate variable $\widehat{\boldsymbol{\eta}}_{\mathrm{A}}$ in the form of their components as $\widehat{\boldsymbol{\eta}}_{\mathrm{A},1} = -\alpha_u\widehat{\Delta}\widehat{\mathbf{u}}_{\mathrm{A},1}$ and $\widehat{\boldsymbol{\eta}}_{\mathrm{A},3} = -\alpha_u\widehat{\Delta}\widehat{\mathbf{u}}_{\mathrm{A},3}$, according to $\widehat{x}_1$ and $\widehat{x}_3$ directions, respectively, as illustrated in Figure 1(a). This setup denotes a 2-dimensional problem. Using this notation, the first set of boundary conditions with $\widehat{\mathbf{u}}_{\mathrm{A}}$ fixed in both directions $\widehat{x}_1$ and $\widehat{x}_3$, can be expressed as

$$\widehat{\mathbf{u}}_{\mathrm{A},k} = \frac{\partial\widehat{\mathbf{u}}_{\mathrm{A},k}}{\partial\widehat{\mathbf{n}}_f} = 0 \quad \text{on } \ \partial\widehat{\Omega}_f\backslash\widehat{\Gamma}_{\mathrm{FSI}}, \quad \text{for } \ k = 1, 3. \tag{19}$$

The first set of boundary conditions acts as clamped edges for a thin plate structure deforming within the fluid domain. For the second type of boundary condition, it is specified to further refine the control over the mesh movement:

$$\begin{array}{llll} \widehat{\mathbf{u}}_{\mathrm{A},1} = \frac{\partial\widehat{\mathbf{u}}_{\mathrm{A},1}}{\partial\widehat{\mathbf{n}}_f} = 0 & \text{and} & \widehat{\boldsymbol{\eta}}_{\mathrm{A},1} = \frac{\partial\widehat{\boldsymbol{\eta}}_{\mathrm{A},1}}{\partial\widehat{\mathbf{n}}_f} = 0 & \text{on } \ \widehat{\Gamma}_{\mathrm{in}} \cup \widehat{\Gamma}_{\mathrm{out}} \\ \widehat{\mathbf{u}}_{\mathrm{A},3} = \frac{\partial\widehat{\mathbf{u}}_{\mathrm{A},3}}{\partial\widehat{\mathbf{n}}_f} = 0 & \text{and} & \widehat{\boldsymbol{\eta}}_{\mathrm{A},3} = \frac{\partial\widehat{\boldsymbol{\eta}}_{\mathrm{A},3}}{\partial\widehat{\mathbf{n}}_f} = 0 & \text{on } \ \widehat{\Gamma}_{\mathrm{sides}} \end{array} . \tag{20}$$

By enforcing zero displacement and its derivative at the boundaries, the second set of boundary conditions restricts the fluid mesh motion perpendicular to the fluid domain's outer boundaries, while allowing deformations along the tangential directions. This specification is effective in minimizing distortions of the fluid cells, leading to enhanced mesh stability and smoother mesh deformation under dynamic FSI conditions. We note that this set of boundary conditions are particularly suited to scenarios where the reference fluid domain $\widehat{\Omega}_f$ is rectangular, such as the depicted fluid domain in Figure 1.

2.4 Equations of motion of the elastic structure

Unlike fluid modeling, structure problems are commonly formulated using Lagrangian coordinates. We use $\widehat{\Omega}_{ss}$ to represent the spatial domain occupied by the purely elastic solid in the reference configuration. The displacement field in Cartesian coordinates, denoted as $\widehat{\mathbf{u}}_{ss}$, is defined as the difference between the positions in the current configuration and the reference configuration, expressed as $\widehat{\mathbf{u}}_{ss}(\widehat{\mathbf{x}}, t) = \mathbf{x} - \widehat{\mathbf{x}}$. Neglecting body forces, the vibration of $\widehat{\Omega}_{ss}$ can be characterized by $\widehat{\mathbf{u}}_{ss}$, which satisfies the elastodynamic equation:

$$\rho_{ss} \frac{\partial^2 \widehat{\mathbf{u}}_{ss}}{\partial t^2} - \widehat{\nabla} \cdot \widehat{\boldsymbol{\Pi}}_{ss} = 0, \quad \text{in } \widehat{\Omega}_{ss}. \tag{21}$$

This equation describes the dynamic equilibrium of the elastic structure under large deformations between the inertial and elastic forces, and represents the conservation of momentum. In this equation, ρ_{ss} is the density of the elastic solid, $\widehat{\boldsymbol{\Pi}}_{ss}$ denotes the First Piola-Kirchhoff stress tensor in the reference configuration, which is often given as the function of Second Piola-Kirchhoff stress tensor:

$$\widehat{\boldsymbol{\Pi}}_{ss} = \widehat{\mathbf{F}}_{ss} \widehat{\boldsymbol{\Sigma}}_{ss} \,, \tag{22}$$

where the deformation gradient $\widehat{\mathbf{F}}_{ss}$ describes both the local rotation and the deformation of the material:

$$\widehat{\mathbf{F}}_{ss} = \mathbf{I} + \widehat{\nabla} \widehat{\mathbf{u}}_{ss} \,. \tag{23}$$

We consider linear elastic material for the solid model, which in terms of the second Piola-Kirchhoff stress tensor $\widehat{\boldsymbol{\Sigma}}_{ss}$ and the Green-Lagrange strain tensor $\widehat{\mathbf{S}}_{ss}$ can be expressed as:

$$\widehat{\boldsymbol{\Sigma}}_{ss} = \mathbb{C}_{ss} : \widehat{\mathbf{S}}_{ss} \,, \tag{24}$$

where the fourth-order elasticity tensor $\mathbb{C}_{ss}$ is given in matrix expressions in 2-dimensional Cartesian coordinates in Appendix A. The Green-Lagrange strain tensor $\widehat{\mathbf{S}}ss$, is defined by:

$$\widehat{\mathbf{S}}_{ss} = \frac{1}{2} \left(\widehat{\mathbf{F}}_{ss}^{\mathrm{T}} \widehat{\mathbf{F}}_{ss} - \mathbf{I} \right) = \frac{1}{2} \left(\widehat{\nabla} \widehat{\mathbf{u}}_{ss} + (\widehat{\nabla} \widehat{\mathbf{u}}_{ss})^{\mathrm{T}} + (\widehat{\nabla} \widehat{\mathbf{u}}_{ss})^{\mathrm{T}} \widehat{\nabla} \widehat{\mathbf{u}}_{ss} \right) . \tag{25}$$

This expression includes the quadratic term associated with geometrical non-linearities. Equilibrium of the solid problem (Eq. 21) is complemented by Dirichlet boundary conditions

$$\widehat{\mathbf{u}}_{ss} = \widehat{\mathbf{g}}_{ss} \,, \quad \text{on } \widehat{\Gamma}_{ss,D} \subset \partial \widehat{\Omega}_{ss} \,, \tag{26}$$

and Neumann boundary conditions

$$\widehat{\boldsymbol{\Pi}}_{ss} \cdot \widehat{\mathbf{n}}_{ss} = \widehat{\mathbf{F}}_{ss} \widehat{\boldsymbol{\Sigma}}_{ss} \cdot \widehat{\mathbf{n}}_{ss} = \widehat{\mathbf{h}}_{ss}, \quad \text{on } \widehat{\Gamma}_{ss,N} \subset \partial \widehat{\Omega}_{ss} \,, \tag{27}$$

applied on the Dirichlet and Neumann boundaries $\widehat{\Gamma}_{ss,D}$ and $\widehat{\Gamma}_{ss,N}$, respectively. Both $\widehat{\mathbf{g}}_{ss}$ and $\widehat{\mathbf{h}}_{ss}$ are prescribed vector functions. $\widehat{\mathbf{n}}ss$ denotes the outward normal vector on the solid boundaries.

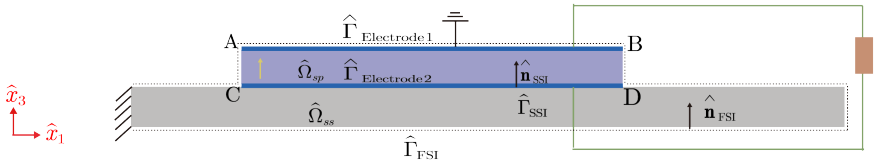

Figure 2: Piezoelectric Energy harvester model scheme.

2.5 Equations of the piezoelectric solid structure

The PFEH system involves piezoelectric patches affixed to the base plate, as depicted in Figure 2. Elastodynamics of the piezoelectric component, occupying the domain $\widehat{\Omega}_{sp}$ in the reference configuration, is provided here. We use $\widehat{\mathbf{u}}_{sp}$ and $\widehat{\boldsymbol{\varphi}}_{sp}$ to denote respectively the displacement field and the electric potential field of $\widehat{\Omega}_{sp}$, in the Cartesian coordinates. The dynamics of $\widehat{\Omega}_{sp}$ is described in terms of both $\widehat{\mathbf{u}}_{sp}$ and $\widehat{\boldsymbol{\varphi}}_{sp}$ via, respectively, the momentum conservation for the mechanical field and the Gauss's equation for the electric field, as

$$\rho_{sp}\frac{\partial^2\widehat{\mathbf{u}}_{sp}}{\partial t^2} - \widehat{\nabla}\cdot\widehat{\boldsymbol{\Pi}}_{sp} = 0, \quad \text{in } \widehat{\Omega}_{sp}\,, \tag{28}$$

$$\widehat{\nabla}\cdot\widehat{\mathbf{D}}_{sp} = 0, \quad \text{in } \widehat{\Omega}_{sp}\,, \tag{29}$$

where ρ_{sp} represents the density of the piezoelectric solid. Unlike the purely elastic solid by Eq. (21), the first Piola-Kirchhoff stress tensor of $\widehat{\Omega}_{sp}$ in the reference configuration, $\widehat{\boldsymbol{\Pi}}_{sp}$, involves piezoelectric effect and results from both $\widehat{\mathbf{u}}_{sp}$ and $\widehat{\boldsymbol{\varphi}}_{sp}$. $\widehat{\mathbf{D}}_{sp}$ denotes the electric displacement. The condition that the divergence of $\widehat{\mathbf{D}}_{sp}$ equals zero indicates that the total flux of electric displacement entering and exiting the domain $\widehat{\Omega}_{sp}$ is in equilibrium, showing the absence of macroscopic charges within the piezoelectric medium. We use linear piezoelectric constitutive relations, which express $\widehat{\boldsymbol{\Pi}}_{sp}$ and $\widehat{\mathbf{D}}_{sp}$ as follows:

$$\widehat{\boldsymbol{\Pi}}_{sp} = \widehat{\mathbf{F}}_{sp}\widehat{\boldsymbol{\Sigma}}_{sp} = \widehat{\mathbf{F}}_{sp}(\mathbb{C}_{sp} : \widehat{\mathbf{S}}_{sp} + \mathbf{e}_{sp}\cdot\widehat{\mathbf{E}}_{sp}), \tag{30}$$

$$\widehat{\mathbf{D}}_{sp} = \mathbf{e}_{sp} : \widehat{\mathbf{S}}_{sp} + \boldsymbol{\epsilon}_{sp}\cdot\widehat{\mathbf{E}}_{sp}\,. \tag{31}$$

The behavior of coupled piezoelectric materials is governed by a set of distinct material properties: the classical fourth-order elastic tensor, $\mathbb{C}_{sp}$, characterizes material elasticity; the second-order tensor, $\boldsymbol{\epsilon}_{sp}$, describes dielectric permittivity; and the third-order piezoelectric coupling tensor, $\mathbf{e}_{sp}$, indicates the electro-mechanical conversion rate. Matrix expressions of these tensors in Cartesian coordinates can be found in Appendix B. The deformation gradient $\widehat{\mathbf{F}}_{sp}$ is derived from the displacement field $\widehat{\mathbf{u}}_{sp}$ within the domain $\widehat{\Omega}_{sp}$ using $\widehat{\mathbf{F}}_{sp} = \mathbf{I} + \widehat{\nabla}\widehat{\mathbf{u}}_{sp}$, identical to purely elastic materials. However, due to the piezoelectric effects, the second Piola-Kirchhoff stress tensor is not only function of the Green-Lagrange strain tensor

but also of the electric field $\widehat{\mathbf{E}}_{sp}$, as indicated in Eq. (24). Similarly, the electric displacement $\widehat{\mathbf{D}}_{sp}$ is dependent on both the electric field and the Green-Lagrange strain. Considering the large deformation, the Green-Lagrange strain $\widehat{\mathbf{S}}_{sp}$ and electric field $\widehat{\mathbf{E}}_{sp}$ are obtained from the displacement field $\widehat{\mathbf{u}}_{sp}$, and the potential field $\widehat{\boldsymbol{\varphi}}_{sp}$, as:

$$\widehat{\mathbf{S}}_{sp} = \frac{1}{2}\left(\widehat{\nabla}\widehat{\mathbf{u}}_{sp} + (\widehat{\nabla}\widehat{\mathbf{u}}_{sp})^{\mathrm{T}} + (\widehat{\nabla}\widehat{\mathbf{u}}_{sp})^{\mathrm{T}}\widehat{\nabla}\widehat{\mathbf{u}}_{sp}\right), \tag{32}$$

$$\widehat{\mathbf{E}}_{sp} = -\widehat{\nabla}\widehat{\boldsymbol{\varphi}}_{sp}\,. \tag{33}$$

The elastodynamics problem of the piezoelectric solid incorporates boundary conditions analogous to those applied to the elastic base plate, as described in Eq. (26) and Eq. (27). In this context, the boundary conditions are expressed for both the displacement field $\widehat{\mathbf{u}}_{sp}$ and the potential field $\widehat{\boldsymbol{\varphi}}_{sp}$. For Dirichlet boundary conditions, this typically involves:

$$\widehat{\mathbf{u}}_{sp} = \widehat{\mathbf{g}}_{sp}\,, \quad \text{on } \widehat{\Gamma}_{sp,uD} \subset \partial\widehat{\Omega}_{sp} \tag{34}$$

$$\widehat{\boldsymbol{\varphi}}_{sp} = \widehat{\mathbf{l}}_{sp}\,, \quad \text{on } \widehat{\Gamma}_{sp,\varphi D} \subset \partial\widehat{\Omega}_{sp} \tag{35}$$

where $\widehat{\Gamma}_{sp,uD}$ and $\widehat{\Gamma}_{sp,\varphi D}$ are the Dirichlet boundaries for $\widehat{\Omega}_{sp}$, where displacement and electric potential conditions are applied, respectively. $\widehat{\mathbf{g}}_{ss}$ and $\widehat{\mathbf{l}}_{sp}$ are the prescribed displacement and potential vector functions. Notably, $\widehat{\Gamma}_{sp,\varphi D}$ specifically corresponds to the electrode surfaces, where the electric potential is maintained uniform. Following this, Neumann boundary conditions can also be implemented:

$$+\widehat{\boldsymbol{\Pi}}_{sp}\cdot\widehat{\mathbf{n}}_{sp} = \widehat{\mathbf{h}}_{sp}, \quad \text{on } \widehat{\Gamma}_{sp,uN} \subset \partial\widehat{\Omega}_{sp}\,, \tag{36}$$

$$-\widehat{\mathbf{D}}_{sp}\cdot\widehat{\mathbf{n}}_{sp} = \widehat{\mathbf{q}}_{sp}, \quad \text{on } \widehat{\Gamma}_{sp,\varphi D} \subset \partial\widehat{\Omega}_{sp}\,, \tag{37}$$

where $\widehat{\Gamma}_{sp,uN}$ and $\widehat{\Gamma}_{sp,\varphi D}$ are the Neumann boundaries, on which prescribed vectors $\widehat{\mathbf{h}}_{sp}$ and $\widehat{\mathbf{q}}_{sp}$ are applied to impose stress and electric displacement conditions, respectively. Then, $\widehat{\mathbf{n}}_{sp}$ denotes the normal vector at the boundaries of $\widehat{\Omega}_{sp}$, pointing outward towards adjacent subdomains. On the lateral surfaces of $\widehat{\Omega}_{sp}$, specifically $\widehat{\Gamma}_{\mathrm{AC}}$ and $\widehat{\Gamma}_{\mathrm{BD}}$ as shown in Figure 2, surface charges are absent ($\widehat{\mathbf{q}}_{sp} = 0$) as piezoelectric materials are insulators.

2.6 Coupling conditions

The energy harvesting system presented in this study requires the consideration of three types of coupling condition. These include fluid-structure interaction (FSI) conditions between the fluid and solid domains ($\widehat{\Omega}_f$ and $\widehat{\Omega}_s$), structure-structure interaction (SSI) conditions between the elastic plate and the piezoelectric solid domains ($\widehat{\Omega}_{ss}$ and $\widehat{\Omega}_{sp}$), and the electrode-external circuit coupling conditions within the domain $\widehat{\Omega}_{sp}$.

Fluid-structure coupling conditions:

We examine the FSI coupling by considering the two involved solid domains, $\widehat{\Omega}_{ss}$ and $\widehat{\Omega}_{sp}$, as a single entity, referred to as $\widehat{\Omega}_s$. Despite their distinct material compositions, the base plate and the piezoelectric component behave similarly when interacting with the surrounding fluid flow. The FSI interface between $\widehat{\Omega}_{ss} \cup \widehat{\Omega}_{sp}$ and the surrounding fluid is denoted as $\widehat{\Gamma}_{\mathrm{FSI}}$, as indicated in Figure 2. At

this interface, we ensure equilibrium by maintaining the continuity of displacement and velocity fields, as well as the normal components of the stress tensor, therefore:

$$\widehat{\mathbf{u}}_{\mathrm{A}} = \widehat{\mathbf{u}}_s, \quad \text{on } \widehat{\Gamma}_{\mathrm{FSI}} \tag{38}$$

$$\widehat{\mathbf{v}}_f = \widehat{\mathbf{v}}_{\mathrm{A}} = \frac{\partial \widehat{\mathbf{u}}_s}{\partial t}, \quad \text{on } \widehat{\Gamma}_{\mathrm{FSI}} \tag{39}$$

$$\left(\boldsymbol{J}_{\mathrm{A}} \widehat{\boldsymbol{\sigma}}_f \mathbf{F}_{\mathrm{A}}^{-\mathbf{T}}\right) \cdot \widehat{\mathbf{n}}_{\mathrm{FSI}} = \widehat{\boldsymbol{\Pi}}_s \cdot \widehat{\mathbf{n}}_{\mathrm{FSI}}, \quad \text{on } \widehat{\Gamma}_{\mathrm{FSI}} \tag{40}$$

where $\widehat{\mathbf{n}}_{\mathrm{FSI}}$ is the normal vector at the FSI interface. We apply the convention that $\widehat{\mathbf{n}}_{\mathrm{FSI}}$ points from $\widehat{\Omega}_f$ towards $\widehat{\Omega}_s$. Ensuring the continuity of displacement and velocity across both the fluid and solid boundaries at the FSI interface guarantees that the fluid meshes deform synchronously with the solid mesh, which prevents the occurrence of overlaps. Consequently, as indicated in Eq. (40), stresses from the fluid and solid domains are transmitted in the direction normal to the FSI interface.

Structure-structure coupling conditions:

We define the SSI coupling conditions at the interface $\widehat{\Gamma}_{\mathrm{SSI}}$, as depicted in Figure 2. This interface connects the elastic base plate domain $\widehat{\Omega}_{ss}$ and the piezoelectric solid domain $\widehat{\Omega}_{sp}$. These conditions are expressed to ensure the continuity of displacement and velocity across $\widehat{\Gamma}_{\mathrm{SSI}}$. We have

$$\widehat{\mathbf{u}}_{ss} = \widehat{\mathbf{u}}_{sp}, \quad \text{on } \widehat{\Gamma}_{\mathrm{SSI}} \tag{41}$$

$$\widehat{\mathbf{v}}_{ss} = \widehat{\mathbf{v}}_{sp}, \quad \text{on } \widehat{\Gamma}_{\mathrm{SSI}} \tag{42}$$

$$\widehat{\boldsymbol{\Pi}}_{ss} \cdot \widehat{\mathbf{n}}_{\mathrm{SSI}} = \widehat{\boldsymbol{\Pi}}_{sp} \cdot \widehat{\mathbf{n}}_{\mathrm{SSI}}, \quad \text{on } \widehat{\Gamma}_{\mathrm{SSI}} \tag{43}$$

where $\widehat{\mathbf{n}}_{\mathrm{SSI}}$ represents the normal vector at the interface $\widehat{\Gamma}_{\mathrm{SSI}}$. By convention, $\widehat{\mathbf{n}}_{\mathrm{SSI}}$ points from the base plate solid domain $\widehat{\Omega}_{ss}$ towards the piezoelectric solid domain $\widehat{\Omega}_{sp}$. The continuity of displacement and velocity across the interface ensures that the piezoelectric element deforms in synchronization with the base plate. The forces acting at the interface, mutually between $\widehat{\Omega}_{ss}$ and $\widehat{\Omega}_{sp}$, are in equilibrium.

Electrode-external circuit coupling conditions:

To harvest the electrical energy generated through the direct piezoelectric effect from the deformation of the piezoelectric component $\widehat{\Omega}_{sp}$, it is necessary to integrate a closed external circuit to the system. In this study, this circuit includes a resistor of resistance R, connected via electric wires to the two electrodes of the piezoelectric component. These electrodes are attached to the upper and the lower surfaces of the piezoelectric patch, denoted by $\widehat{\Gamma}_{\mathrm{Electrode1}} := \widehat{\Gamma}_{\mathrm{AB}}$ and $\widehat{\Gamma}_{\mathrm{Electrode2}} := \widehat{\Gamma}_{\mathrm{CD}}$, respectively. The integrated system setup is illustrated in Figure 2. The electrodes, which are extremely thin, allow the accumulation of free electric charges and ensure uniform potential distribution across their surfaces during the deformation of the piezoelectric component. In this resistive circuit, Ohm's law establishes the relationship between the electric current flowing through the conductor between points, and the voltage across it, expressed as:

$$\widehat{\varphi}_{sp} = RI\,. \tag{44}$$

The potential difference developed across the two electrodes is equivalent to the potential across the resistor. Consequently, the electric current passing through the upper electrode, based on the conservation

of charge, is described by:

$$I = -\frac{\partial Q}{\partial t}\,, \tag{45}$$

where I denotes the current flowing through the circuit, and Q the total electric charges accumulated on the electrode-covered surfaces. This formulation represents the principle of charge conservation, that in a closed circuit, the current corresponds to the rate at which electric charge changes over time.

3 Monolithic solution scheme

This section will focus on the resolution of the fluid-structure-piezoelectric coupling problem using a monolithic solution approach. Employing the Galerkin finite element method in the reference configuration, the objective is to analyze the dynamics and energy harvesting capabilities of the coupled system using FEniCS. Temporal discretization employs finite difference schemes, in particular the One-Step-θ method. Given the inclusion of a closed circuit in the system, special emphasis will be placed on effectively addressing the electric energy consumption of the circuit and the modeling of electrodes within the FEniCS platform.

3.1 Weak forms for single fields

We present the governing equations of each subdomain composing the FSI system in the form of their weak formulation. These formulations are important for the numerical implementation of PDE systems and their boundary conditions via the finite element method, which we will use for numerical resolution. Some notations will be used, such as $(\quad,\quad)_{\widehat{\Omega}}$ for scalar product in the domain $\widehat{\Omega}$, and $<\quad,\quad>_{\widehat{\Gamma}}$ for scalar product on the boundary $\widehat{\Gamma}$. We will then present the weak forms for the different domains as follows:

Fluid domain: Focusing on the equilibrium of the fluid domain $\widehat{\Omega}_f$ during the time interval $[0, T]$, the dynamic behavior is described by its ALE form NS equations (Eqs. (12) and (13)) under the influence of the boundary conditions given by Eq. (40). Using the Galerkin method, we solve the unknowns $\widehat{\mathbf{v}}_f$ and $\widehat{p}_f$. Let $\widehat{\boldsymbol{\psi}}_f^{\widehat{\mathbf{v}}}$ and $\widehat{\psi}_f^{\widehat{p}}$ be the test functions that we use to multiply with Eqs. (12) and (13). We then proceed with the integration over the respective domain using Green's formula, which leads to the weak form of the elastodynamic governing equation for the fluid domain in its reference configuration, with the account for FSI effets, as expressed in Eq. (46):

$$\begin{aligned}
&+\left(\rho_f \widehat{\boldsymbol{J}}_{\mathrm{A}} \tfrac{\partial \widehat{\mathbf{v}}_f}{\partial t}, \widehat{\boldsymbol{\psi}}_f^{\widehat{\mathbf{v}}}\right)_{\widehat{\Omega}_f} + \left(\rho_f \widehat{\boldsymbol{J}}_{\mathrm{A}} \widehat{\mathbf{F}}_{\mathrm{A}}^{-1} \left(\widehat{\mathbf{v}}_f - \widehat{\mathbf{v}}_{\mathrm{A}}\right) \cdot \nabla \widehat{\mathbf{v}}_f, \widehat{\boldsymbol{\psi}}_f^{\widehat{\mathbf{v}}}\right)_{\widehat{\Omega}_f} + \left(\widehat{\boldsymbol{J}}_{\mathrm{A}} \widehat{\boldsymbol{\sigma}}_f \widehat{\mathbf{F}}_{\mathrm{A}}^{-\mathrm{T}}, \widehat{\nabla} \widehat{\boldsymbol{\psi}}_f^{\widehat{\mathbf{v}}}\right)_{\widehat{\Omega}_f} \\
&- \left(\widehat{\boldsymbol{J}}_{\mathrm{A}} \widehat{\boldsymbol{\sigma}}_f \widehat{\mathbf{F}}_{\mathrm{A}}^{-\mathrm{T}} \cdot \widehat{\mathbf{n}}_{\mathrm{FSI}}, \widehat{\nabla} \widehat{\boldsymbol{\psi}}_f^{\widehat{\mathbf{v}}}\right)_{\widehat{\Gamma}_{\mathrm{FSI}}} = 0 \quad \forall \widehat{\boldsymbol{\psi}}_f^{\widehat{\mathbf{v}}}, \\
&+\left(\nabla \cdot \left(\widehat{\boldsymbol{J}}_{\mathrm{A}} \widehat{\mathbf{F}}_{\mathrm{A}}^{-1} \widehat{\mathbf{v}}_f\right), \widehat{\psi}_f^{\widehat{p}}\right)_{\widehat{\Omega}_f} = 0 \quad \forall \widehat{\psi}_f^{\widehat{p}},
\end{aligned} \tag{46}$$

where $\widehat{\mathbf{v}}_{\mathrm{A}} = \frac{\partial \widehat{\mathbf{u}}_{\mathrm{A}}}{\partial t}$ represents the auxiliary velocity associated with the fluid mesh motion, which should be distinguished from $\widehat{\mathbf{v}}_f$. Integration by parts is applied to Eq. $(46-1)$ to obtain relaxed continuity requirement for $\widehat{\mathbf{v}}_f$, an operation not repeated in Eq. $(46-2)$. Similarly, weak formulations for the mesh extension problem using biharmonic model are obtained by integrating Eq. (18) multiplied by

test functions $\widehat{\boldsymbol{\psi}}^{\widehat{\boldsymbol{\eta}}}_{\mathrm{A}}$ and $\widehat{\boldsymbol{\psi}}^{\widehat{\mathbf{u}}}_{\mathrm{A}}$ over the fluid domain $\widehat{\Omega}_f$,

$$
\begin{aligned}
&+\left(\widehat{\boldsymbol{\eta}}_{\mathrm{A}}, \widehat{\boldsymbol{\psi}}^{\widehat{\boldsymbol{\eta}}}_{\mathrm{A}}\right)_{\widehat{\Omega}_f} - \left(\alpha_u \widehat{\nabla}\widehat{\mathbf{u}}_{\mathrm{A}}, \widehat{\nabla}\widehat{\boldsymbol{\psi}}^{\widehat{\boldsymbol{\eta}}}_{\mathrm{A}}\right)_{\widehat{\Omega}_f} = 0 \quad \forall \widehat{\boldsymbol{\psi}}^{\widehat{\boldsymbol{\eta}}}_{\mathrm{A}}, \\
&+\left(\alpha_u \widehat{\nabla}\widehat{\boldsymbol{\eta}}_{\mathrm{A}}, \widehat{\nabla}\widehat{\boldsymbol{\psi}}^{\widehat{\mathbf{u}}}_{\mathrm{A}}\right)_{\widehat{\Omega}_f} = 0 \quad \forall \widehat{\boldsymbol{\psi}}^{\widehat{\mathbf{u}}}_{\mathrm{A}}.
\end{aligned}
\tag{47}
$$

The introduction of these weak formulations will enable us to effectively implement the fluid dynamics and mesh deformation problems while ensuring numerical stability.

Elastic solid domain: Correspondingly, the dynamic behavior of the pure elastic solid domain (the base plate, $\widehat{\Omega}_{ss}$) is governed by the equation of momentum conservation (Eq. (21)) under the influence of FSI conditions defined in Eq. (40), and SSI conditions defined in Eq. (43), associated with the interfaces $\widehat{\Gamma}_{\mathrm{FSI}}$ and $\widehat{\Gamma}_{\mathrm{SSI}}$, respectively. Adopting a similar approach as described in the previous section, we solve $\widehat{\mathbf{v}}_{ss}$ and $\widehat{\mathbf{u}}_{ss}$, and let $\widehat{\boldsymbol{\psi}}^{\widehat{\mathbf{v}}}_{ss}$ and $\widehat{\boldsymbol{\psi}}^{\widehat{\mathbf{u}}}_{ss}$ be the test functions. Subsequently, we introduce the integral expression of the elastodynamics governing equation for the elastic solid domain $\widehat{\Omega}_{ss}$, involving FSI and SSI conditions, as stated in Eq. (48):

$$
\begin{aligned}
&+\left(\rho_{ss}\tfrac{\partial \widehat{\mathbf{v}}_{ss}}{\partial t}, \widehat{\boldsymbol{\psi}}^{\widehat{\mathbf{v}}}_{ss}\right)_{\widehat{\Omega}_{ss}} + \left(\widehat{\boldsymbol{\Pi}}_{ss}, \widehat{\nabla}\widehat{\boldsymbol{\psi}}^{\widehat{\mathbf{v}}}_{ss}\right)_{\widehat{\Omega}_{ss}} + \left\langle \widehat{\boldsymbol{\Pi}}_{ss}\cdot\widehat{\mathbf{n}}_{\mathrm{FSI}}, \widehat{\boldsymbol{\psi}}^{\widehat{\mathbf{v}}}_{ss}\right\rangle_{\widehat{\Gamma}_{\mathrm{FSI}}} - \left\langle \widehat{\boldsymbol{\Pi}}_{ss}\cdot\widehat{\mathbf{n}}_{\mathrm{SSI}}, \widehat{\boldsymbol{\psi}}^{\widehat{\mathbf{v}}}_{ss}\right\rangle_{\widehat{\Gamma}_{\mathrm{SSI}}} = 0 \quad \forall \widehat{\boldsymbol{\psi}}^{\widehat{\mathbf{v}}}_{ss}, \\
&+\left(\rho_{ss}\left(\tfrac{\partial \widehat{\mathbf{u}}_{ss}}{\partial t} - \widehat{\mathbf{v}}_{ss}\right), \widehat{\boldsymbol{\psi}}^{\widehat{\mathbf{u}}}_{ss}\right)_{\widehat{\Omega}_{ss}} = 0 \quad \forall \widehat{\boldsymbol{\psi}}^{\widehat{\mathbf{u}}}_{ss}
\end{aligned}
\tag{48}
$$

In Eq. (48-1), the third term has an opposite sign compared to Eq. (46-1). This is due to the orientation of the normal vector $\widehat{\mathbf{n}}_{\mathrm{FSI}}$, which is defined to be opposite to that of $\widehat{\mathbf{n}}_{\mathrm{ss}}$ as given in Eq. (40) from Section 2.6. In addition, to ensure consistency across the treatment of both solid and fluid problems, particularly in maintaining the same first order of time, which simplifies subsequent time discretization, a supplementary solid velocity variable $\widehat{\mathbf{v}}_{ss}$ is introduced, with relationships expressed in Eq. (48-2).

Piezoelectric solid domain: With similar method as described for Eq. (48), we develop the weak formulations for the piezoelectric solid domain $\widehat{\Omega}_{sp}$ based on the momentum conservation equations (Eq. (28) and Eq. (29)). The problem is complemented by FSI and SSI boundary conditions (Eqs. (40),(43)), the electrode conditions associated with the homogenization of potential field on the electrode surfaces, and the resistor based circuit relations (Eqs. (37), (44) and (45)). We solve $\widehat{\mathbf{v}}_{sp}$, $\widehat{\mathbf{u}}_{sp}$, $\widehat{\boldsymbol{\psi}}_{sp}$ and $\widehat{\boldsymbol{\varphi}}_{sp}$, using test functions $\widehat{\boldsymbol{\psi}}^{\widehat{\mathbf{v}}}_{sp}$, $\widehat{\boldsymbol{\psi}}^{\widehat{\mathbf{u}}}_{sp}$, $\widehat{\boldsymbol{\psi}}^{\widehat{\boldsymbol{\varphi}}}_{sp}$ and $\widehat{\boldsymbol{\psi}}^{\widehat{\boldsymbol{\phi}}}_{sp}$. The weak formulation is expressed as follows:

$$
\begin{aligned}
&+\left(\rho_{sp}\tfrac{\partial \widehat{\mathbf{v}}_{sp}}{\partial t}, \widehat{\boldsymbol{\psi}}^{\widehat{\mathbf{v}}}_{sp}\right)_{\widehat{\Omega}_{sp}} + \left(\widehat{\boldsymbol{\Pi}}_{sp}, \widehat{\nabla}\widehat{\boldsymbol{\psi}}^{\widehat{\mathbf{v}}}_{sp}\right)_{\widehat{\Omega}_{sp}} + \left\langle \widehat{\boldsymbol{\Pi}}_{sp}\cdot\widehat{\mathbf{n}}_{\mathrm{FSI}}, \widehat{\boldsymbol{\psi}}^{\widehat{\mathbf{v}}}_{sp}\right\rangle_{\widehat{\Gamma}_{\mathrm{FSI}}} + \left\langle \widehat{\boldsymbol{\Pi}}_{sp}\cdot\widehat{\mathbf{n}}_{\mathrm{SSI}}, \widehat{\boldsymbol{\psi}}^{\widehat{\mathbf{v}}}_{sp}\right\rangle_{\widehat{\Gamma}_{\mathrm{SSI}}} = 0 \quad \forall \widehat{\boldsymbol{\psi}}^{\widehat{\mathbf{v}}}_{sp} \\
&+\left(\rho_{sp}\left(\tfrac{\partial \widehat{\mathbf{u}}_{sp}}{\partial t} - \widehat{\mathbf{v}}_{sp}\right), \widehat{\boldsymbol{\psi}}^{\widehat{\mathbf{u}}}_{sp}\right)_{\widehat{\Omega}_{sp}} = 0 \quad \forall \widehat{\boldsymbol{\psi}}^{\widehat{\mathbf{u}}}_{sp} \\
&-\left(\widehat{\mathbf{D}}_{sp}, \widehat{\nabla}\widehat{\boldsymbol{\psi}}^{\widehat{\boldsymbol{\phi}}}_{sp}\right)_{\widehat{\Omega}_{sp}} + \left\langle \beta\widehat{\nabla}\widehat{\boldsymbol{\varphi}}_{sp}, \widehat{\mathbf{D}}_{sp}\Big|_{\widehat{\boldsymbol{\psi}}^{\widehat{\mathbf{v}}}_{sp}, \widehat{\boldsymbol{\psi}}^{\widehat{\boldsymbol{\phi}}}_{sp}}\right\rangle_{\widehat{\Gamma}_{\mathrm{Electrode2}}} - \left\langle \widehat{\mathbf{D}}_{sp}\cdot\widehat{\mathbf{n}}_{sp}, \widehat{\boldsymbol{\psi}}^{\widehat{\boldsymbol{\phi}}}_{sp}\right\rangle_{\widehat{\Gamma}_{\mathrm{Electrode2}}} = 0 \quad \forall \widehat{\boldsymbol{\psi}}^{\widehat{\mathbf{v}}}_{sp}, \widehat{\boldsymbol{\psi}}^{\widehat{\boldsymbol{\phi}}}_{sp} \\
&+\left(\left(\tfrac{\partial \widehat{\boldsymbol{\varphi}}_{sp}}{\partial t} - \widehat{\boldsymbol{\phi}}_{sp}\right), \widehat{\boldsymbol{\psi}}^{\widehat{\boldsymbol{\varphi}}}_{sp}\right)_{\widehat{\Omega}_{sp}} = 0 \quad \forall \widehat{\boldsymbol{\psi}}^{\widehat{\boldsymbol{\varphi}}}_{sp}\,.
\end{aligned}
\tag{49}
$$

Considering the definition of the normals $\widehat{\mathbf{n}}_{\mathrm{FSI}}$ and $\widehat{\mathbf{n}}_{\mathrm{SSI}}$, the signs of the third and fourth terms in Eq. (49-1) are reversed. In addition to the solid velocity $\widehat{\mathbf{v}}_{sp}$ provided in this part, we also introduce the

potential rate $\widehat{\dot{\boldsymbol{\phi}}}_{sp}$, which is the time derivative of the potential $\widehat{\boldsymbol{\varphi}}_{sp}$. This addition ensures consistency in the physical interpretation of the terms in Eq. (49-3) with those in Eq. (49-1), specifically in terms of virtual power.

Some remarks are necessary regarding Eq. (49-3), particularly in how electrodes are integrated into the resistor-based electric circuit. The primary function of the electrodes is to ensure a uniform distribution of electric potential across the piezoelectric solid surface, on which the induced potential presents typically non-uniform distribution. To achieve uniform evolution of the potential across the electrode surfaces, we propose to employ a penalty technique to the second term in Eq. (48-3). This term, $\widehat{\mathbf{D}}_{sp}\Big|_{\widehat{\boldsymbol{\psi}}^{\hat{\mathbf{v}}}_{sp},\widehat{\boldsymbol{\psi}}^{\hat{\boldsymbol{\phi}}}_{sp}}$ recasts the variables of electrical displacement from $\widehat{\mathbf{u}}_{sp}$ and $\widehat{\boldsymbol{\varphi}}_{sp}$ into the test functions $\widehat{\boldsymbol{\psi}}^{\hat{\mathbf{v}}}_{sp}$ and $\widehat{\boldsymbol{\psi}}^{\hat{\boldsymbol{\phi}}}_{sp}$. By setting the constant coefficient β to a high value, such as 10^7, we significantly amplify the rate of electric field energy, causing the potential gradient $\widehat{\nabla}\widehat{\boldsymbol{\varphi}}_{sp}$ to approach zero, ensuring nearly uniform potential across the electrode surface. This approach allows modeling the electrode behavior without introducing additional physical entities. Moreover, concerning the third term in Eq. (49-3), we formulate a specific expression for $\widehat{\mathbf{D}}_{sp}\cdot\widehat{\mathbf{n}}_{sp}$ considering the resistor-based circuit. Let us recall the Neumann boundary condition in Eq. (37) and apply it across the electrode surface $\widehat{\Gamma}_{\text{Electrode2}}$:

$$-\left\langle \widehat{\mathbf{D}}_{sp}\cdot\widehat{\mathbf{n}}_{sp}, \widehat{\boldsymbol{\psi}}^{\hat{\boldsymbol{\phi}}}_{sp}\right\rangle_{\widehat{\Gamma}_{\text{Electrode2}}} = \left\langle \widehat{\mathbf{q}}_{sp}, \widehat{\boldsymbol{\psi}}^{\hat{\boldsymbol{\phi}}}_{sp}\right\rangle_{\widehat{\Gamma}_{\text{Electrode2}}}, \tag{50}$$

where $\widehat{\mathbf{q}}_{sp}$ represents the electric charge density, which is calculated from the total electric charge Q collected on the electrode surface, using the relationship $\widehat{\mathbf{q}}_{sp} = Q/\mathrm{A}$, where A denotes the electrode surface area. From Eqs. (44) and (45), we derive that $\frac{\partial Q}{\partial t} = -\widehat{\boldsymbol{\varphi}}_{sp}/R$. Over the time interval T, the total electric charge is given by:

$$Q = \int_0^T -\widehat{\boldsymbol{\varphi}}_{sp}/R \,\mathrm{dt}\,. \tag{51}$$

If we consider $(n+1)$ time steps $t_1, t_2, \ldots, t_n, t_{n+1}$ with a constant time step interval $\Delta t = t_{n+1} - t_n$, where the results up to the n-th time step are known, and the $(n+1)$-th time step is currently being calculated, Eq. (51) can be simplified to:

$$Q^{n+1} = -\frac{\Delta t}{R}\widehat{\boldsymbol{\varphi}}^{n+1}_{sp} + Q^n, \tag{52}$$

where Q^n represents the electric charge accumulated over n time steps, calculated as $Q^n = \sum_{i=1}^{n} -\frac{\Delta t}{R}\widehat{\boldsymbol{\varphi}}^{i}_{sp}$. This approach requires the potential to be integrable and continuous over the period T, so that it remains bounded within the interval to allow accurate integration, typically necessary for computing accumulated quantities over time. With Eqs. (50), (51) and (52), the exact formulation for the circuit term in Eq. (49-3) is thus expressed as:

$$-\left\langle \widehat{\mathbf{D}}_{sp}\cdot\widehat{\mathbf{n}}_{sp}, \widehat{\boldsymbol{\psi}}^{\hat{\boldsymbol{\phi}}}_{sp}\right\rangle_{\widehat{\Gamma}_{\text{Electrode2}}} = \left\langle -\frac{\Delta t}{R\mathrm{A}}\widehat{\boldsymbol{\varphi}}^{n+1}_{sp} + \frac{Q^n}{\mathrm{A}}, \widehat{\boldsymbol{\psi}}^{\hat{\boldsymbol{\phi}}}_{sp}\right\rangle_{\widehat{\Gamma}_{\text{Electrode2}}}. \tag{53}$$

Incorporating Eq. (53) integrates the resistor-based closed circuit into the PFEH system. This inclusion allows for the quantification of electrical energy harvested from the kinetic energy of fluid flow. Concurrently, alterations in the electric field within the piezoelectric solid, as a result of the energy-consuming resistor, will affect the structural stiffness of the PFEH system, thus its dynamics. This mutual effect leads to complex, fully coupled, multi-physical interactions, which are important to consider when evaluating the system's overall functionality.

3.2 Weak forms for whole coupled PFEH system

After developing the weak formulations for the fluid-structure-piezoelectric coupled system within their respective domains, we now transition to unified formulations using the classic monolithic FSI framework. This method involves treating the fluid and structural domains as a single, surface-coupled physical entity. Within this unified framework, the velocity field $\widehat{\mathbf{v}}$ and the displacement field $\widehat{\mathbf{u}}$ are defined continuously across all the domains in their reference configurations. It is important to note that in the fluid domain, the displacement field is not directly associated with the velocity field. The relationships between variables in the unified and individual domains are expressed as follows:

$$\widehat{\mathbf{v}} = \begin{cases} \widehat{\mathbf{v}}_f & \text{in } \widehat{\Omega}_f \\ \widehat{\mathbf{v}}_{ss} & \text{in } \widehat{\Omega}_{ss} \\ \widehat{\mathbf{v}}_{sp} & \text{in } \widehat{\Omega}_{sp} \end{cases} . \tag{54}$$

$$\widehat{\mathbf{u}} = \begin{cases} \widehat{\mathbf{u}}_{\mathrm{A}} & \text{in } \widehat{\Omega}_f \\ \widehat{\mathbf{u}}_{ss} & \text{in } \widehat{\Omega}_{ss} \\ \widehat{\mathbf{u}}_{sp} & \text{in } \widehat{\Omega}_{sp} \end{cases} . \tag{55}$$

In the domain $\widehat{\Omega}$ and considering the time interval T, we express the variational formulation of the coupled system in a simplied form, with the objective to solve $\widehat{\boldsymbol{U}} = \{\widehat{\mathbf{v}}, \widehat{\mathbf{u}}, \widehat{\boldsymbol{\eta}}_{\mathrm{A}}, \widehat{p}, \widehat{\boldsymbol{\varphi}}, \widehat{\boldsymbol{\phi}}\}$ using the test functions $\widehat{\boldsymbol{\Psi}} = \{\widehat{\boldsymbol{\psi}}^{\widehat{\mathbf{v}}}, \widehat{\boldsymbol{\psi}}^{\widehat{\mathbf{u}}}, \widehat{\boldsymbol{\psi}}^{\widehat{\boldsymbol{\eta}}}_{\mathrm{A}}, \widehat{\boldsymbol{\psi}}^{\widehat{p}}, \widehat{\boldsymbol{\psi}}^{\widehat{\boldsymbol{\varphi}}}, \widehat{\boldsymbol{\psi}}^{\widehat{\boldsymbol{\phi}}}\}$, as follows:

$$\int_0^T \widehat{\boldsymbol{A}}(\widehat{\boldsymbol{U}})(\widehat{\boldsymbol{\Psi}})\mathrm{d}t = \int_0^T \widehat{\boldsymbol{b}}(\widehat{\boldsymbol{\Psi}})\mathrm{d}t \quad \forall \widehat{\boldsymbol{\Psi}} \, . \tag{56}$$

Disregarding the body forces, the right-hand side term $\widehat{\boldsymbol{b}}(\widehat{\boldsymbol{\Psi}}) = \left(\rho_s \widehat{\boldsymbol{f}}_s, \widehat{\boldsymbol{\psi}}^{\widehat{\mathbf{v}}}\right)_{\widehat{\Omega}_s}$ equals zero. By combining Eqs (46)–(53), we formulate the "truly monolithic" weak form for the coupled problem across the entire domain $\widehat{\Omega} = \widehat{\Omega}_f \cup \widehat{\Omega}_{ss} \cup \widehat{\Omega}_{sp}$, which leads to:

$$\begin{aligned}
&\widehat{\boldsymbol{A}}(\widehat{\boldsymbol{U}})(\widehat{\boldsymbol{\Psi}}) = \\
&+ \left(\rho_f \boldsymbol{J}_{\mathrm{A}} \tfrac{\partial \widehat{\mathbf{v}}}{\partial t}, \widehat{\boldsymbol{\psi}}^{\widehat{\mathbf{v}}}\right)_{\widehat{\Omega}_f} + \left(\rho_f \boldsymbol{J}_{\mathrm{A}} \mathbf{F}_{\mathrm{A}}^{-1} \left(\widehat{\mathbf{v}} - \tfrac{\partial \widehat{\mathbf{u}}}{\partial t}\right) \cdot \nabla \widehat{\mathbf{v}}, \widehat{\boldsymbol{\psi}}^{\widehat{\mathbf{v}}}\right)_{\widehat{\Omega}_f} + \left(\boldsymbol{J}_{\mathrm{A}} \widehat{\boldsymbol{\sigma}}_f \mathbf{F}_{\mathrm{A}}^{-\mathrm{T}}, \widehat{\nabla} \widehat{\boldsymbol{\psi}}^{\widehat{\mathbf{v}}}\right)_{\widehat{\Omega}_f} \\
&- \left(\boldsymbol{J}_{\mathrm{A}} \widehat{\boldsymbol{\sigma}}_f \mathbf{F}_{\mathrm{A}}^{-\mathrm{T}} \cdot \widehat{\mathbf{n}}_{\mathrm{FSI}}, \widehat{\nabla} \widehat{\boldsymbol{\psi}}^{\widehat{\mathbf{v}}}\right)_{\widehat{\Gamma}_{\mathrm{FSI}}} + \left(\nabla \cdot \left(\widehat{\boldsymbol{J}}_{\mathrm{A}} \widehat{\mathbf{F}}_{\mathrm{A}}^{-1} \widehat{\mathbf{v}}\right), \widehat{\boldsymbol{\psi}}^{\widehat{p}}\right)_{\widehat{\Omega}_f} \\
&+ \left(\widehat{\boldsymbol{\eta}}_{\mathrm{A}}, \widehat{\boldsymbol{\psi}}^{\widehat{\boldsymbol{\eta}}}_{\mathrm{A}}\right)_{\widehat{\Omega}_f} - \left(\alpha_u \widehat{\nabla} \widehat{\mathbf{u}}, \widehat{\nabla} \widehat{\boldsymbol{\psi}}^{\widehat{\boldsymbol{\eta}}}_{\mathrm{A}}\right)_{\widehat{\Omega}_f} + \left(\alpha_u \widehat{\nabla} \widehat{\boldsymbol{\eta}}_{\mathrm{A}}, \widehat{\nabla} \widehat{\boldsymbol{\psi}}^{\widehat{\mathbf{u}}}\right)_{\widehat{\Omega}_f} \\
&+ \left(\rho_{ss} \tfrac{\partial \widehat{\mathbf{v}}}{\partial t}, \widehat{\boldsymbol{\psi}}^{\widehat{\mathbf{v}}}\right)_{\widehat{\Omega}_{ss}} + \left(\widehat{\boldsymbol{\Pi}}_{ss}, \widehat{\nabla} \widehat{\boldsymbol{\psi}}^{\widehat{\mathbf{v}}}\right)_{\widehat{\Omega}_{ss}} + \left\langle \widehat{\boldsymbol{\Pi}}_{ss} \cdot \widehat{\mathbf{n}}_{\mathrm{FSI}}, \widehat{\boldsymbol{\psi}}^{\widehat{\mathbf{v}}} \right\rangle_{\widehat{\Gamma}_{\mathrm{FSI}}} - \left\langle \widehat{\boldsymbol{\Pi}}_{ss} \cdot \widehat{\mathbf{n}}_{\mathrm{SSI}}, \widehat{\boldsymbol{\psi}}^{\widehat{\mathbf{v}}} \right\rangle_{\widehat{\Gamma}_{\mathrm{SSI}}} + \left(\rho_{ss} \left(\tfrac{\partial \widehat{\mathbf{u}}}{\partial t} - \widehat{\mathbf{v}}\right), \widehat{\boldsymbol{\psi}}^{\widehat{\mathbf{u}}}\right)_{\widehat{\Omega}_{ss}} \\
&+ \left(\rho_{sp} \tfrac{\partial \widehat{\mathbf{v}}}{\partial t}, \widehat{\boldsymbol{\psi}}^{\widehat{\mathbf{v}}}\right)_{\widehat{\Omega}_{sp}} + \left(\widehat{\boldsymbol{\Pi}}_{sp}, \widehat{\nabla} \widehat{\boldsymbol{\psi}}^{\widehat{\mathbf{v}}}\right)_{\widehat{\Omega}_{sp}} + \left\langle \widehat{\boldsymbol{\Pi}}_{sp} \cdot \widehat{\mathbf{n}}_{\mathrm{FSI}}, \widehat{\boldsymbol{\psi}}^{\widehat{\mathbf{v}}} \right\rangle_{\widehat{\Gamma}_{\mathrm{FSI}}} + \left\langle \widehat{\boldsymbol{\Pi}}_{sp} \cdot \widehat{\mathbf{n}}_{\mathrm{SSI}}, \widehat{\boldsymbol{\psi}}^{\widehat{\mathbf{v}}} \right\rangle_{\widehat{\Gamma}_{\mathrm{SSI}}} + \left(\rho_{sp} \left(\tfrac{\partial \widehat{\mathbf{u}}}{\partial t} - \widehat{\mathbf{v}}\right), \widehat{\boldsymbol{\psi}}^{\widehat{\mathbf{u}}}\right)_{\widehat{\Omega}_{sp}} \\
&- \left(\widehat{\mathbf{D}}_{sp}, -\widehat{\nabla} \widehat{\boldsymbol{\psi}}^{\widehat{\boldsymbol{\phi}}}\right)_{\widehat{\Omega}_{sp}} + \left\langle -\beta \widehat{\nabla} \widehat{\boldsymbol{\varphi}}, \widehat{\mathbf{D}}_{sp} \Big|_{\widehat{\boldsymbol{\psi}}^{\widehat{\mathbf{v}}}, \widehat{\boldsymbol{\psi}}^{\widehat{\boldsymbol{\phi}}}} \right\rangle_{\widehat{\Gamma}_{\mathrm{electrode}}} + \left\langle -\tfrac{\Delta t}{R\mathrm{A}} \widehat{\boldsymbol{\varphi}} + \tfrac{Q^n}{\mathrm{A}}, \widehat{\boldsymbol{\psi}}^{\widehat{\boldsymbol{\phi}}} \right\rangle_{\widehat{\Gamma}_{\mathrm{electrode}}} + \left(\left(\tfrac{\partial \widehat{\boldsymbol{\varphi}}}{\partial t} - \widehat{\boldsymbol{\phi}}\right), \widehat{\boldsymbol{\psi}}^{\widehat{\boldsymbol{\varphi}}}\right)_{\widehat{\Omega}_{sp}} \\
&= 0 \quad \forall \widehat{\boldsymbol{\psi}}^{\widehat{\mathbf{v}}}, \widehat{\boldsymbol{\psi}}^{\widehat{\mathbf{u}}}, \widehat{\boldsymbol{\psi}}^{\widehat{\boldsymbol{\eta}}}_{\mathrm{A}}, \widehat{\boldsymbol{\psi}}^{\widehat{p}}, \widehat{\boldsymbol{\psi}}^{\widehat{\boldsymbol{\varphi}}}, \widehat{\boldsymbol{\psi}}^{\widehat{\boldsymbol{\phi}}}
\end{aligned} \tag{57}$$

Eq. (57) requires solving six different variables, which include, the global velocity $\widehat{\mathbf{v}}$ and displacement $\widehat{\mathbf{u}}$ across $\widehat{\Omega}$, the intermediate mesh variable $\widehat{\boldsymbol{\eta}}_{\mathrm{A}}$ within $\widehat{\Omega}_f$, fluid pressure $\widehat{p}$ in $\widehat{\Omega}_f$, and both electric

potential $\widehat{\varphi}$ and electric potential rate $\widehat{\phi}$ in $\widehat{\Omega}_{sp}$. It is important to note that, while the domains form a unified entity, they are distinctively identified for each component, as illustrated in Figure 3 (a) and (b). At each interface, specifically on the FSI and SSI boundaries, mesh nodes are fully shared, ensuring satisfaction of continuity conditions. Consequently, integral terms associated with the FSI and SSI boundaries are omitted from Eq. (57) in the following.

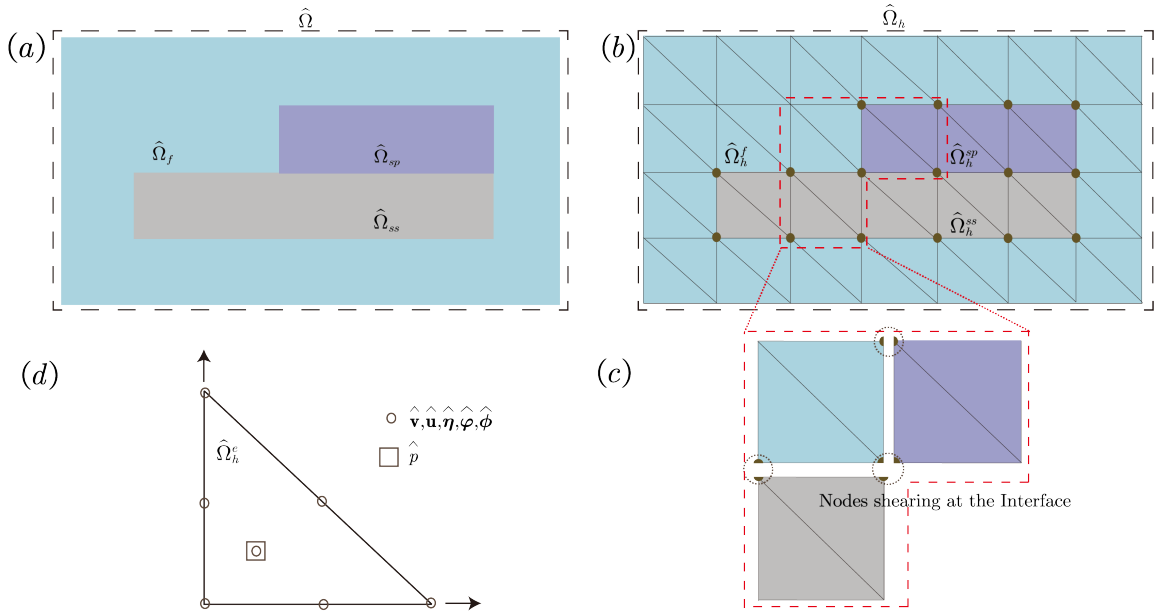

Figure 3: Monolithic computational mesh: (a) illustration of the continuous spatial domains (b) the discretized domain representation (c) interface elements (d) Q_2^c, P_1^{dc} isoparametric finite element.

3.3 Time discretization method

Following the presentation of truly monolithic weak formulations in Section 3.2, the subsequent step involves discretizing these formulations within finite-dimensional subspaces. This leads to semi-discrete equations ready for numerical resolution through an appropriate time discretization scheme. In this study, we utilize the implicit One-Step-θ method, which offers flexibility to treat both stationary and time-dependent solutions depending on the chosen θ value. For a generic variable $\boldsymbol{a}$, the One-Step-θ method for the $(n+1)$th time step is formulated as:

$$\left[\frac{\partial \boldsymbol{a}}{\partial t} + f(\boldsymbol{a})\right]^{n+1} = 0 \quad \rightarrow \quad \frac{\boldsymbol{a}^{n+1} - \boldsymbol{a}^n}{\Delta t} + \theta[f(\boldsymbol{a})]^{n+1} + (1-\theta)[f(\boldsymbol{a})]^n = 0 \tag{58}$$

Three values of θ are commonly employed according to specific problem-solving requirements. For stationary solutions, setting $\theta = 1$ and $\Delta t \rightarrow +\infty$ aligns with the Euler scheme. This method is unconditionally stable but offers only first-order time accuracy. For time-dependent solutions, the Crank-Nicolson scheme, with $\theta = 1/2$, provides second-order time accuracy but may encounter instabilities with challenging initial and boundary data. A variant, the Shifted Crank-Nicolson scheme ($\theta = 1/2 + \Delta t$), ensures global stability but at the expense of second-order accuracy, which is the approach adopted in this study.

The implementation of the Shifted Crank-Nicolson scheme begins by defining $\widehat{\boldsymbol{A}}(\widehat{\boldsymbol{U}})(\widehat{\boldsymbol{\Psi}})$ and grouping these into four categories based on terms in Eq. (57): time equation terms $\widehat{\boldsymbol{A}}_T(\widehat{\boldsymbol{U}})(\widehat{\boldsymbol{\Psi}})$, implicit terms $\widehat{\boldsymbol{A}}_I(\widehat{\boldsymbol{U}})(\widehat{\boldsymbol{\Psi}})$ (always kept implicit, such as fluid incompressibility), pressure terms $\widehat{\boldsymbol{A}}_P(\widehat{\boldsymbol{U}})(\widehat{\boldsymbol{\Psi}})$, circuit terms $\widehat{\boldsymbol{A}}_C(\widehat{\boldsymbol{U}})(\widehat{\boldsymbol{\Psi}})$, and all remaining terms $\widehat{\boldsymbol{A}}_E(\widehat{\boldsymbol{U}})(\widehat{\boldsymbol{\Psi}})$ (including stress terms, convection, etc.), which leads to:

$$\begin{aligned}\widehat{\boldsymbol{A}}_T(\widehat{\boldsymbol{U}})(\widehat{\boldsymbol{\Psi}}) = &+\left(\rho_f \boldsymbol{J}_{\mathrm{A}}\frac{\partial\widehat{\mathbf{v}}}{\partial t},\widehat{\boldsymbol{\psi}}^{\widehat{\mathbf{v}}}\right)_{\widehat{\Omega}_f}-\left(\rho_f \boldsymbol{J}_{\mathrm{A}}\mathbf{F}_{\mathrm{A}}^{-1}\frac{\partial\widehat{\mathbf{u}}}{\partial t}\cdot\nabla\widehat{\mathbf{v}},\widehat{\boldsymbol{\psi}}^{\widehat{\mathbf{v}}}\right)_{\widehat{\Omega}_f}\\&+\left(\rho_{ss}\frac{\partial\widehat{\mathbf{v}}}{\partial t},\widehat{\boldsymbol{\psi}}^{\widehat{\mathbf{v}}}\right)_{\widehat{\Omega}_{ss}}+\left(\rho_{ss}\frac{\partial\widehat{\mathbf{u}}}{\partial t},\widehat{\boldsymbol{\psi}}^{\widehat{\mathbf{u}}}\right)_{\widehat{\Omega}_{ss}}+\left(\rho_{sp}\frac{\partial\widehat{\mathbf{v}}}{\partial t},\widehat{\boldsymbol{\psi}}^{\widehat{\mathbf{v}}}\right)_{\widehat{\Omega}_{sp}}+\left(\rho_{sp}\frac{\partial\widehat{\mathbf{u}}}{\partial t},\widehat{\boldsymbol{\psi}}^{\widehat{\mathbf{u}}}\right)_{\widehat{\Omega}_{sp}}+\left(\frac{\partial\widehat{\boldsymbol{\varphi}}}{\partial t},\widehat{\boldsymbol{\psi}}^{\widehat{\boldsymbol{\varphi}}}\right)_{\widehat{\Omega}_{sp}},\end{aligned}\tag{59}$$

$$\widehat{\boldsymbol{A}}_I(\widehat{\boldsymbol{U}})(\widehat{\boldsymbol{\Psi}}) = +\left(\nabla\cdot\left(\widehat{\boldsymbol{J}}_{\mathrm{A}}\widehat{\mathbf{F}}_{\mathrm{A}}^{-1}\widehat{\mathbf{v}}\right),\widehat{\boldsymbol{\psi}}^{\widehat{p}}\right)_{\widehat{\Omega}_f}+\left(\widehat{\boldsymbol{\eta}}_{\mathrm{A}},\widehat{\boldsymbol{\psi}}_{\mathrm{A}}^{\widehat{\boldsymbol{\eta}}}\right)_{\widehat{\Omega}_f}-\left(\alpha_u\widehat{\nabla}\widehat{\mathbf{u}},\widehat{\nabla}\widehat{\boldsymbol{\psi}}_{\mathrm{A}}^{\widehat{\boldsymbol{\eta}}}\right)_{\widehat{\Omega}_f}+\left(\alpha_u\widehat{\nabla}\widehat{\boldsymbol{\eta}}_{\mathrm{A}},\widehat{\nabla}\widehat{\boldsymbol{\psi}}^{\widehat{\mathbf{u}}}\right)_{\widehat{\Omega}_f},\tag{60}$$

$$\widehat{\boldsymbol{A}}_P(\widehat{\boldsymbol{U}})(\widehat{\boldsymbol{\Psi}}) = +\left(\boldsymbol{J}_{\mathrm{A}}\widehat{\boldsymbol{\sigma}}_{fp}\mathbf{F}_{\mathrm{A}}^{-\mathrm{T}},\widehat{\nabla}\widehat{\boldsymbol{\psi}}^{\widehat{\mathbf{v}}}\right)_{\widehat{\Omega}_f},\tag{61}$$

$$\widehat{\boldsymbol{A}}_C(\widehat{\boldsymbol{U}})(\widehat{\boldsymbol{\Psi}}) = +\left\langle-\frac{\Delta t}{R\mathrm{A}}\widehat{\boldsymbol{\varphi}}+\frac{Q^n}{\mathrm{A}},\widehat{\boldsymbol{\psi}}^{\widehat{\boldsymbol{\phi}}}\right\rangle_{\widehat{\Gamma}_{\mathrm{Electrode2}}},\tag{62}$$

$$\begin{aligned}\widehat{\boldsymbol{A}}_E(\widehat{\boldsymbol{U}})(\widehat{\boldsymbol{\Psi}}) = &+\left(\rho_f \boldsymbol{J}_{\mathrm{A}}\mathbf{F}_{\mathrm{A}}^{-1}\widehat{\mathbf{v}}\cdot\nabla\widehat{\mathbf{v}},\widehat{\boldsymbol{\psi}}^{\widehat{\mathbf{v}}}\right)_{\widehat{\Omega}_f}+\left(\boldsymbol{J}_{\mathrm{A}}\widehat{\boldsymbol{\sigma}}_{fv}\mathbf{F}_{\mathrm{A}}^{-\mathrm{T}},\widehat{\nabla}\widehat{\boldsymbol{\psi}}^{\widehat{\mathbf{v}}}\right)_{\widehat{\Omega}_f}\\&+\left(\widehat{\boldsymbol{\Pi}}_{ss},\widehat{\nabla}\widehat{\boldsymbol{\psi}}^{\widehat{\mathbf{v}}}\right)_{\widehat{\Omega}_{ss}}-\left(\rho_{ss}\widehat{\mathbf{v}},\widehat{\boldsymbol{\psi}}^{\widehat{\mathbf{u}}}\right)_{\widehat{\Omega}_{ss}}+\left(\widehat{\boldsymbol{\Pi}}_{sp},\widehat{\nabla}\widehat{\boldsymbol{\psi}}^{\widehat{\mathbf{v}}}\right)_{\widehat{\Omega}_{sp}}-\left(\rho_{sp}\widehat{\mathbf{v}},\widehat{\boldsymbol{\psi}}^{\widehat{\mathbf{u}}}\right)_{\widehat{\Omega}_{sp}}\\&-\left(\widehat{\mathbf{D}}_{sp},-\widehat{\nabla}\widehat{\boldsymbol{\psi}}^{\widehat{\boldsymbol{\phi}}}\right)_{\widehat{\Omega}_{sp}}+\left\langle-\beta\widehat{\nabla}\widehat{\boldsymbol{\varphi}},\widehat{\mathbf{D}}_{sp}\Big|_{\widehat{\boldsymbol{\psi}}^{\widehat{\mathbf{v}}},\widehat{\boldsymbol{\psi}}^{\widehat{\boldsymbol{\phi}}}}\right\rangle_{\widehat{\Gamma}_{\mathrm{Electrode2}}}-\left(\widehat{\boldsymbol{\phi}},\widehat{\boldsymbol{\psi}}^{\widehat{\boldsymbol{\varphi}}}\right)_{\widehat{\Omega}_{sp}},\end{aligned}\tag{63}$$

in which the reduced tensors $\widehat{\boldsymbol{\sigma}}_{fp}$ and $\widehat{\boldsymbol{\sigma}}_{fv}$ are expressed as: $\widehat{\boldsymbol{\sigma}}_{fp}=-\widehat{p}_f\mathbf{I}$, $\widehat{\boldsymbol{\sigma}}_{fv}=+\rho_f\mu_f\left((\nabla\widehat{\mathbf{v}})\,\widehat{\mathbf{F}}_{\mathrm{A}}^{-1}+\widehat{\mathbf{F}}_{\mathrm{A}}^{-\mathrm{T}}\,(\nabla\widehat{\mathbf{v}})^{\mathrm{T}}\right)$. Specifically, the time derivative terms in $\widehat{\boldsymbol{A}}_T(\widehat{\boldsymbol{U}})$ can be treated by a backward difference quotient. For the time step t^{n+1}, we will compute $\widehat{\mathbf{v}}:=\widehat{\mathbf{v}}^{n+1}$, $\widehat{\mathbf{u}}:=\widehat{\mathbf{u}}^{n+1}$, $\widehat{\boldsymbol{\varphi}}:=\widehat{\boldsymbol{\varphi}}^{n+1}$ through:

$$\begin{aligned}&\widehat{\boldsymbol{A}}_T\left(\widehat{\boldsymbol{U}}\right)(\widehat{\boldsymbol{\Psi}})\approx\widehat{\boldsymbol{A}}_T\left(\widehat{\boldsymbol{U}}^{n+1,k}\right)(\widehat{\boldsymbol{\Psi}})\\&=+\left(\rho_f\widehat{\boldsymbol{J}}_{\mathrm{A}}^{n+1,\theta}\tfrac{\widehat{\mathbf{v}}-\widehat{\mathbf{v}}^n}{\Delta t},\widehat{\boldsymbol{\psi}}^{\widehat{\mathbf{v}}}\right)_{\widehat{\Omega}_f}-\left(\rho_f\widehat{\boldsymbol{J}}_{\mathrm{A}}\widehat{\mathbf{F}}_{\mathrm{A}}^{-1}\tfrac{\widehat{\mathbf{u}}-\widehat{\mathbf{u}}^n}{\Delta t}\cdot\widehat{\nabla}\widehat{\mathbf{v}},\widehat{\boldsymbol{\psi}}^{\widehat{\mathbf{v}}}\right)_{\widehat{\Omega}_f}\\&+\left(\rho_{ss}\tfrac{\widehat{\mathbf{v}}-\widehat{\mathbf{v}}^n}{\Delta t},\widehat{\boldsymbol{\psi}}^{\widehat{\mathbf{v}}}\right)_{\widehat{\Omega}_{ss}}+\left(\rho_{ss}\tfrac{\widehat{\mathbf{u}}-\widehat{\mathbf{u}}^n}{\Delta t},\widehat{\boldsymbol{\psi}}^{\widehat{\mathbf{u}}}\right)_{\widehat{\Omega}_{ss}}\\&+\left(\rho_{sp}\tfrac{\widehat{\mathbf{v}}-\widehat{\mathbf{v}}^n}{\Delta t},\widehat{\boldsymbol{\psi}}^{\widehat{\mathbf{v}}}\right)_{\widehat{\Omega}_{sp}}+\left(\rho_{sp}\tfrac{\widehat{\mathbf{u}}-\widehat{\mathbf{u}}^n}{\Delta t},\widehat{\boldsymbol{\psi}}^{\widehat{\mathbf{u}}}\right)_{\widehat{\Omega}_{sp}}+\left(\tfrac{\widehat{\boldsymbol{\varphi}}-\widehat{\boldsymbol{\varphi}}^n}{\Delta t},\widehat{\boldsymbol{\psi}}^{\widehat{\boldsymbol{\varphi}}}\right)_{\widehat{\Omega}_{sp}},\end{aligned}\tag{64}$$

where the $\widehat{\boldsymbol{J}}_{\mathrm{A}}^{n+1,\theta}$ is based on the interpolation expression: $\widehat{\boldsymbol{J}}_{\mathrm{A}}^{n+1,\theta}=\theta\widehat{\boldsymbol{J}}_{\mathrm{A}}^{n+1}+(1-\theta)\widehat{\boldsymbol{J}}_{\mathrm{A}}^{n}$. With the former time step given by $\widehat{\mathbf{v}}^n:=\widehat{\mathbf{v}}(t^n)$, $\widehat{\mathbf{u}}^n:=\widehat{\mathbf{u}}(t^n)$, $\widehat{\boldsymbol{\varphi}}^n:=\widehat{\boldsymbol{\varphi}}(t^n)$, we will obtain the solution $\widehat{\boldsymbol{U}}^{n+1}=\{\widehat{\mathbf{v}}^{n+1},\widehat{\mathbf{u}}^{n+1},\widehat{\boldsymbol{\eta}}_{\mathrm{A}}^{n+1},\widehat{p}^{n+1},\widehat{\boldsymbol{\varphi}}^{n+1},\widehat{\boldsymbol{\phi}}^{n+1}\}$, such that:

$$\widehat{\boldsymbol{A}}_T\left(\widehat{\boldsymbol{U}}^{n+1,k}\right)(\widehat{\boldsymbol{\Psi}})+\theta\widehat{\boldsymbol{A}}_E\left(\widehat{\boldsymbol{U}}^{n+1}\right)(\widehat{\boldsymbol{\Psi}})+\widehat{\boldsymbol{A}}_P\left(\widehat{\boldsymbol{U}}^{n+1}\right)(\widehat{\boldsymbol{\Psi}})+\widehat{\boldsymbol{A}}_C\left(\widehat{\boldsymbol{U}}^{n+1}\right)(\widehat{\boldsymbol{\Psi}})+\widehat{\boldsymbol{A}}_I\left(\widehat{\boldsymbol{U}}^{n+1}\right)(\widehat{\boldsymbol{\Psi}})$$
$$=-(1-\theta)\widehat{\boldsymbol{A}}_E\left(\widehat{\boldsymbol{U}}^{n}\right)(\widehat{\boldsymbol{\Psi}})+\theta\widehat{\boldsymbol{b}}^{n+1}(\widehat{\boldsymbol{\Psi}})+(1-\theta)\widehat{\boldsymbol{b}}^{n}(\widehat{\boldsymbol{\Psi}}) \tag{65}$$

With Eq. (65), we have completed the time discretization process. The remaining terms to be resolved are on the left-hand side of the equation, representing the unknowns to be solved. The right-hand side contains the already calculated quantities from the previous time step, represented by $\widehat{\boldsymbol{U}}^n = \widehat{\mathbf{v}}^n, \widehat{\mathbf{u}}^n, \widehat{\boldsymbol{\eta}}_{\mathrm{A}}^n, \widehat{p}^n, \widehat{\boldsymbol{\varphi}}^n, \widehat{\boldsymbol{\phi}}^n$.

3.4 Spatial discretization method

Following time discretization, the next step involves spatial discretization of the equations using the finite element Galerkin method. This method will be applied within the continuous spatial domains designated as $\widehat{\Omega} = \widehat{\Omega}_f \cup \widehat{\Omega}_{ss} \cup \widehat{\Omega}_{sp}$. Each of these domains, $\widehat{\Omega}_f$, $\widehat{\Omega}_{ss}$, and $\widehat{\Omega}_{sp}$, represents a distinct subdomain. To numerically solve these equations, the continuous spatial domain is approximated by a discrete domain $\widehat{\Omega}_h$, divided into open cells with polygonal boundaries. The set of trilaterals covering $\widehat{\Omega}_h$ is denoted as $\widehat{\mathcal{T}}_h$. Each regular trilateral in $\widehat{\mathcal{T}}_h$ represents an element $\widehat{\Omega}_h^e$ in the discretized domain, as depicted in Figure 3 $(c)-(d)$. The assumption of regularity ensures that any two trilaterals in $\widehat{\mathcal{T}}_h$ are either disjoint or share only a common vertex or edge.

It is important to choose appropriate finite element spaces within the trilaterals $\widehat{\mathcal{T}}_h$. The chosen finite element spaces should conform to the monolithic approach, which requires consistent usage of finite elements throughout the fluid and solid regions composing the system. Given the incompressibility of all materials involved, we have selected a specific pair of finite element spaces, Q_2^c, P_1^{dc}, typically utilized for problems with incompressibility constraints [38, 39]. This choice not only ensures stability but also maintains consistency in addressing incompressibility across the system, leading to effective and coherent numerical resolution. The reference trilaterals for this configuration are denoted by $\overline{\widehat{\mathbb{T}}}^2 = [0,1]^2$. The spaces $\mathcal{U}, \mathcal{V}, \mathcal{W}, \mathcal{X}, \mathcal{Y}, \mathcal{P}$ over the interval $[t_n, t_{n+1}]$ are thus approximated by the Q_2^c, P_1^{dc} pair as follows:

$$\begin{aligned}
\mathcal{U}_h &= \left\{\widehat{\mathbf{u}}_h \in \left[C\left(\widehat{\Omega}_h\right)\right]^2, \widehat{\mathbf{u}}_h|_{\widehat{\mathbb{T}}} \in \left[Q_2^c(\widehat{\mathbb{T}})\right]^2 \quad \forall \widehat{\mathbb{T}} \in \mathcal{T}_h, \widehat{\mathbf{u}_h} = 0 \quad \text{on } \widehat{\Gamma}_D\right\} \\
\mathcal{V}_h &= \left\{\widehat{\mathbf{v}}_h \in \left[C\left(\widehat{\Omega}_h\right)\right]^2, \widehat{\mathbf{v}}_h|_{\widehat{\mathbb{T}}} \in \left[Q_2^c(\widehat{\mathbb{T}})\right]^2 \quad \forall \widehat{\mathbb{T}} \in \mathcal{T}_h, \widehat{\mathbf{v}}_h = 0 \quad \text{on } \widehat{\Gamma}_D\right\} \\
\mathcal{W}_h &= \left\{\widehat{\boldsymbol{\eta}}_h \in \left[C\left(\widehat{\Omega}_h\right)\right]^2, \widehat{\boldsymbol{\eta}}_h|_{\widehat{\mathbb{T}}} \in \left[Q_2^c(\widehat{\mathbb{T}})\right]^2 \quad \forall \widehat{\mathbb{T}} \in \mathcal{T}_h, \widehat{\boldsymbol{\eta}}_h = 0 \quad \text{on } \widehat{\Gamma}_D\right\} \\
\mathcal{X}_h &= \left\{\widehat{\boldsymbol{\varphi}}_h \in C\left(\widehat{\Omega}_h\right), \widehat{\boldsymbol{\varphi}}_h|_{\widehat{\mathbb{T}}} \in Q_2^c(\widehat{\mathbb{T}}) \quad \forall \widehat{\mathbb{T}} \in \mathcal{T}_h, \widehat{\boldsymbol{\varphi}}_h = 0 \quad \text{on } \widehat{\Gamma}_D\right\} \\
\mathcal{Y}_h &= \left\{\widehat{\boldsymbol{\phi}}_h \in C\left(\widehat{\Omega}_h\right), \widehat{\boldsymbol{\phi}}_h\Big|_{\widehat{\mathbb{T}}} \in Q_2^c(\widehat{\mathbb{T}}) \quad \forall \widehat{\mathbb{T}} \in \mathcal{T}_h, \widehat{\boldsymbol{\phi}}_h = 0 \quad \text{on } \widehat{\Gamma}_D\right\} \\
\mathcal{P}_h &= \left\{\widehat{p}_h \in L^2\left(\widehat{\Omega}_h\right), \widehat{p_h}|_{\widehat{\mathbb{T}}} \in P_1^{dc}(\widehat{\mathbb{T}}) \quad \forall \widehat{\mathbb{T}} \in \mathcal{T}_h\right\}
\end{aligned} \tag{66}$$

In this set of finite element spaces, $\widehat{\mathbf{u}}_h, \widehat{\mathbf{v}}_h, \widehat{\boldsymbol{\eta}}_h$ are vector fields where, in a 2-dimensional problem setup, each node possesses two degrees of freedom. Instead, for the scalar fields such as $\widehat{\boldsymbol{\varphi}}_h, \widehat{\boldsymbol{\phi}}_h$ and $\widehat{p}_h$, each

node is assigned only one degree of freedom. In this study, to achieve consistent high precision for the electrical variables, which include the potential and potential rate fields, compared to the mechanical variables, which include the displacement and velocity fields, we continue to use the Q_2^c element for the discretization of both the potential and potential rate fields.

3.5 Solution algorithm

After completing the space discretization with the Galerkin method and time discretization with the shifted Crank-Nicolson scheme, we arrive at a nonlinear algebraic set of equations. These equations are constructed using the basis of finite element spaces $\mathcal{U}_h, \mathcal{V}_h, \mathcal{W}_h, \mathcal{X}_h, \mathcal{Y}_h, \mathcal{P}_h$, and their corresponding test function spaces $\widehat{\boldsymbol{\psi}}^{\widehat{\mathbf{v}}}, \widehat{\boldsymbol{\psi}}^{\widehat{\mathbf{u}}}, \widehat{\boldsymbol{\psi}}_{\mathrm{A}}^{\widehat{\boldsymbol{\eta}}}, \widehat{\boldsymbol{\psi}}^{\widehat{p}}, \widehat{\boldsymbol{\psi}}^{\widehat{\boldsymbol{\varphi}}}, \widehat{\boldsymbol{\psi}}^{\widehat{\phi}}$. For each time step, our aim is to find the solution vector: $\widehat{\boldsymbol{U}}^{n+1} = \{\widehat{\mathbf{v}}_h^{n+1}, \widehat{\mathbf{u}}_h^{n+1}, \widehat{\boldsymbol{\eta}}_h^{n+1}, \widehat{p}_h^{n+1}, \widehat{\boldsymbol{\varphi}}_h^{n+1}, \widehat{\phi}_h^{n+1}\} \in \mathcal{U}_h \times \mathcal{V}_h \times \mathcal{W}_h \times \mathcal{X}_h \times \mathcal{Y}_h \times \mathcal{P}_h$, as defined by:

$$\widehat{\boldsymbol{\mathcal{F}}}\left(\widehat{\boldsymbol{U}}\right) = 0\,. \tag{67}$$

This equation $\widehat{\boldsymbol{\mathcal{F}}}$ represents the system described in Eq. (65), which incorporates nonlinearities from the fluid's convective term and the solid's geometric equations. To address the resolution of the system, we employ the Newton method, which offers an iterative algorithm combining simplicity and broad applicability. Notably, quadratic convergence can be achieved when the initial guess is sufficiently close to the solution. One Newton iteration for solving the system of nonlinear algebraic equations can be represented as:

$$\widehat{\boldsymbol{U}}^{n+1} = \widehat{\boldsymbol{U}}^{n} - \delta\widehat{\boldsymbol{U}}\,. \tag{68}$$

Steps for implementing one iteration according to the Newton method:

- **Initial guess**: Start with an initial guess for $\widehat{\boldsymbol{U}}^n$.
- **Evaluate residual and gradients**: Calculate the residuum $\widehat{\boldsymbol{\mathcal{R}}}^n = \widehat{\boldsymbol{\mathcal{F}}}(\widehat{\boldsymbol{U}}^n)$ and its gradient matrix $\widehat{\boldsymbol{\mathcal{A}}} = \frac{\partial\widehat{\boldsymbol{\mathcal{F}}}}{\partial\widehat{\boldsymbol{U}}}(\widehat{\boldsymbol{U}}^n)$.
- **Newton correction**: Determine the Newton correction step with $\delta\widehat{\boldsymbol{U}} = (\widehat{\boldsymbol{\mathcal{A}}})^{-1}\widehat{\boldsymbol{\mathcal{R}}}^n$.
- **Update solution**: Update the solution $\widehat{\boldsymbol{U}}^{n+1} = \widehat{\boldsymbol{U}}^n - \left[\frac{\partial\widehat{\boldsymbol{\mathcal{F}}}}{\partial\widehat{\boldsymbol{U}}}(\widehat{\boldsymbol{U}}^n)\right]^{-1}\widehat{\boldsymbol{\mathcal{F}}}(\widehat{\boldsymbol{U}}^n)$.
- **Stopping criteria**: Check for convergence by examining the magnitude of the Newton correction. Terminate the iteration if changes are within acceptable limits or a predefined maximum number of iterations is reached.

With all discretization methods and solution strategies implemented on the FEniCS platform, we are ready to conduct validations and simulations using the developed fluid-structure-piezoelectric coupled model for PFEH.

4 Validations

In this section, we validate the nonlinear monolithic solution scheme developed in Section 3 through a two-part analysis. The first part addresses fluid-structure interaction cases with geometric nonlinearities. We employ the well-established 2D benchmark problems, specifically FSI3, as proposed by Turek

and Hron [19]. In the second part, we move our focus to piezoelectric structures coupled with an output circuit to take into account the direct piezoelectric effect. Here, we simulate a purely piezoelectric solid structure subjected to harmonic external loads. The electrical output is compared with results obtained from the commercial finite element software, COMSOL [40].

All simulations were performed using the open-source environment, FEniCS [31] and its extension, TurtleFSI [41]. We implemented the governing equations of the piezoelectric fluid energy harvesting system, as described in the previous sections, within FEniCS, which then solves the equations based on the finite element method. TurtleFSI is a FEniCS extension designed for general fluid-structure interaction problems. In this work, TurtleFSI has been extended to accommodate more complex coupled problems, such as the integration of fluid-structure-piezoelectric coupling with an external electric circuit, as depicted in Figure 4.

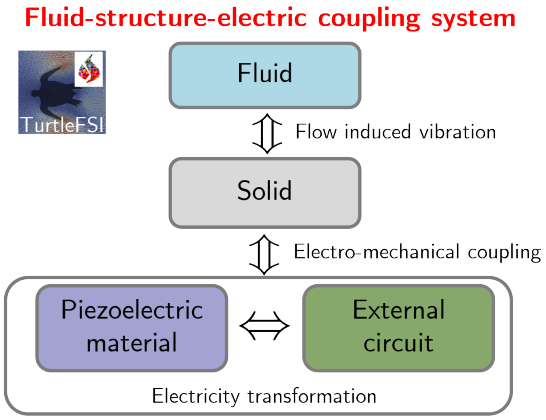

Figure 4: The relations between different components of the coupling system

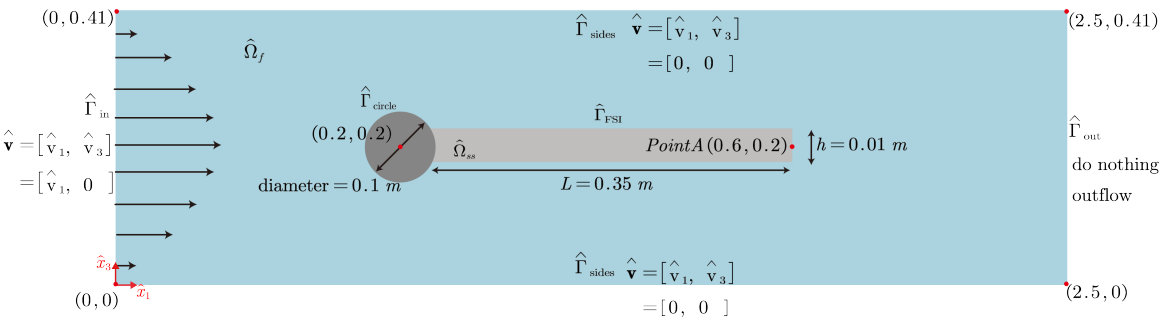

Figure 5: Geometry and boundary conditions of benchmark case FSI3

4.1 Validation of the FSI system

Previously, TurtleFSI has been used predominantly for general fluid-structure interaction problems but has not been applied to piezoelectric systems in scenarios involving flow-induced vibrations. The aim of this case study is to evaluate its compatibility with typical flow-induced vibration system architectures for energy harvesting. These systems usually consist of a slender vibrating structure connected to a

Table 1: Material parameters from FSI3

Domain	$\widehat{\Omega}_{ss}$			$\widehat{\Omega}_f$		
Parameter	ρ_{ss} (kg/m^3)	c_{11} (MPa)	c_{12} (MPa)	ρ_f (kg/m^3)	μ_f (kg/(m $\cdot$ s))	$\overline{\mathrm{v}}$ (m/s)
Value	1000	12	8	1000	1	2

Table 2: Case configurations from FSI3

Case name	Δt (s)	Mesh name	Mesh number
FSI3-(1)	0.1	Mesh-level2	7689
FSI3-(2)	0.02	Mesh-level2	7689
FSI3-(3)	0.01	Mesh-level2	7689
FSI3-(4)	0.001	Mesh-level2	7689
FSI3-(5)	0.01	Mesh-level1	4133
FSI3-(6)	0.01	Mesh-level3	15646
FSI3-(7)	0.01	Mesh-level4	29395

bluff-body-based vortex generator under steady or unsteady fluid flow conditions. Before implementing integrated electromechanical coupling, it is important to validate the associate modeling techniques, ranging from model parameter settings to finite element discretization, against established benchmarks in the literature. In this regard, we utilize the FSI3 benchmark, which focuses on the flow-induced vibrations of a slender elastic structure involving large deformations, located downstream of a rigid circular cylinder within a channel flow. The geometry of the physical problem is depicted in Figure 5. Point A $(0.6, 0.2)$, situated at the center of the structure's free end, is used as the control point for data extraction. The origin of the axes is positioned at the bottom-left corner node of the fluid domain. This intentionally asymmetrical setup is intended to prevent any reliance on computational precision for triggering potential oscillations.

The detailed physical parameters for both the fluid and solid domains are provided in Table 1. The solid domain utilizes a Saint-Venant Kirchhoff material, known for its elastic properties, to form a solid plate positioned behind a cylinder with sharp corners. Concurrently, the fluid domain is characterized by a viscous flow with a Reynolds number of $Re = 200$, calculated based on the cylinder's diameter and the average inflow velocity. This configuration leads to unsteady vortex shedding in the wake of the cylinder, resulting in dynamic fluid-structure interaction scenarios.

Concerning the boundary conditions, a parabolic inflow velocity profile is implemented at the inlet, defined as:

$$\widehat{\mathrm{v}}_1 = \begin{cases} 1.5\overline{\mathrm{v}}\frac{\widehat{x}_3(0.41-\widehat{x}_3)}{(0.41/2)^2}\frac{1-\cos(0.5\pi t)}{2}, & \text{if } t < 2 \\ 1.5\overline{\mathrm{v}}\frac{\widehat{x}_3(0.41-\widehat{x}_3)}{(0.41/2)^2}, & \text{otherwise} \end{cases}, \tag{69}$$

where $\overline{\mathrm{v}}$ is the mean inflow velocity, set at 2 m/s for this benchmark. No-slip conditions are applied on the top and bottom channel walls as well as on the rigid circular surface. At the outlet, a zero normal stress boundary condition is enforced.

Validation cases are conducted across varying time steps and mesh densities, as outlined in Table 2. Cases FSI3-(1) through FSI3-(4) utilize a consistent mesh (Mesh-level2) but with decreasing time steps from 0.1 to 0.001 s. Cases FSI3-(5) through FSI3-(7) examine increasing mesh densities across the

entire computational domain, illustrated in Figure 6.

Dependence on the time step and mesh refinement levels is compared in in Table 3 and 4, as well as in Figure 7. We focus on parameters which include displacements in directions $\widehat{x}_1$ and $\widehat{x}_3$, denoted as $\widehat{\mathrm{u}}_1$ and $\widehat{\mathrm{u}}_3$ respectively, that we measure at point A $(0.6, 0.2)$. Aerodynamic drag and lift coefficients, C_d and C_l, for the entire bluff-body are also examined. The results are confronted against benchmark cases based on various strongly coupling methods provided in the review by Turek et al. [42], which utilize the identical time step $\Delta t = 0.01\,\mathrm{s}$ across different methods.

According to Table 3 and Figure 7(a), a time step of 0.1 s is excessively large since it results in no vibrations. Nonetheless, the solver remains stable, showing the robustness of the shifted Crank-Nicolson scheme. Then, reducing the time step to 0.01 s and smaller leads to consistent, self-sustained, periodic oscillations. The minor differences observed in the results comparing the time steps 0.01 s and 0.001 s indicate that a $\times 10$ increase in the number of time steps, thus in computational cost, does not proportionately enhance the accuracy. Meanwhile, from Table 4 and Figure 7(b), an increase in mesh density shows only a marginal impact on the outcomes, with results remaining nearly consistent above Mesh-level1. A slight time delay is observed in Mesh-level1 compared to denser meshes. Among the seven cases, Case FSI3-(3) with a time step of 0.01 s and Mesh-level2 offers an optimal balance between computational expense and accuracy, aligning well with data from the reference groups. In conclusion, the TurtleFSI environment and the presented modeling setup have demonstrated their compatibility with the modeling of flow-induced vibration systems, typically employed in energy harvesting applications.

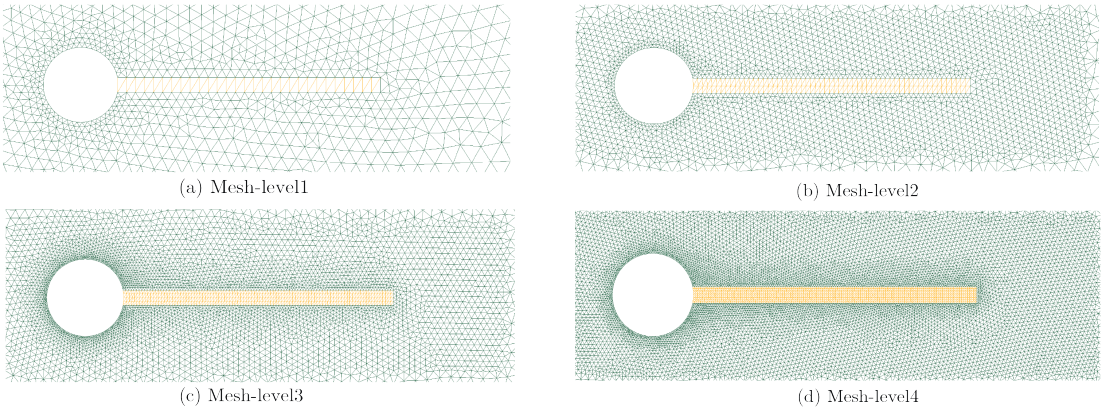

Figure 6: Four meshes densities of benchmark case FSI3

4.2 Validation of Piezoelectric Coupling

Following the evaluation of the FSI behavior for the flow-induced vibrator model, this section moves attention to the modeling of piezoelectric components. Representing electromechanical coupling accurately is essential for developing an integrated electromechanical system with FSI. To validate our model, we compare results with those obtained from the commercial software COMSOL. Our focus is on analyzing both the vibration and electrical output of a structure composed entirely of piezoelectric material, which is connected to a resistor-based circuit. The model uses a 2-dimensional plane strain approach, and features $\widehat{x}_3$-polarization as illustrated in Figure 8. The piezoelectric structure is clamped along the lower surface. Both the upper and lower surfaces of the piezoelectric structure coincide with

Table 3: Validation for time independence

	Δt (s)	$\widehat{\mathrm{u}}_1$ of PointA (m)	$\widehat{\mathrm{u}}_3$ of PointA (m)	C_d	C_l
FSI3-(1)	0.1	-0.0006±0.0000	0.0116±0.0001	2.283±0.000	1.429±0.002
FSI3-(2)	0.02	-0.0026±0.0027	0.0021±0.0348	2.351±0.263	0.002±0.906
FSI3-(3)	0.01	-0.0024±0.0023	0.0013±0.0320	2.266±0.091	0.010±0.625
FSI3-(4)	0.001	-0.0025±0.0024	0.0014±0.0351	2.273±0.101	0.014±0.629
ref-Turek		-0.0029±0.0027	0.0015±0.0349	2.293±0.136	0.010±0.767
ref-Schafer		-0.0027±0.0025	0.0015±0.0344	2.286±0.113	0.011±0.749
ref-Rannacher		-0.0028±0.0027	0.0012±0.0346	2.262±0.131	0.012±0.764
ref-Wall		-0.0020±0.0019	0.0014±0.0290	2.170±0.088	0.013±0.881

Table 4: Validation for mesh independence

	Mesh	$\widehat{\mathrm{u}}_1$ of PointA (m)	$\widehat{\mathrm{u}}_3$ of PointA (m)	C_d	C_l
FSI3-(5)	Mesh-level1	-0.0024±0.0023	0.0016±0.0319	2.230±0.076	0.010+-0.632
FSI3-(3)	Mesh-level2	-0.0024±0.0023	0.0013±0.0320	2.266±0.091	0.010±0.625
FSI3-(6)	Mesh-level3	-0.0024±0.0022	0.0013±0.0320	2.290±0.094	0.012±0.656
FSI3-(7)	Mesh-level4	-0.0024±0.0022	0.0014±0.0320	2.292±0.095	0.019±0.660
ref-Turek		-0.0029±0.0027	0.0015±0.0349	2.293±0.136	0.010±0.767
ref-Schafer		-0.0027±0.0025	0.0015±0.0344	2.286±0.113	0.011±0.749
ref-Rannacher		-0.0028±0.0027	0.0012±0.0346	2.262±0.131	0.012±0.764
ref-Wall		-0.0020±0.0019	0.0014±0.0290	2.170±0.088	0.013±0.881

the respective electrodes $\widehat{\Gamma}_{\text{electrode2}}$ and $\widehat{\Gamma}_{\text{electrode1}}$. The lower electrode surface $\widehat{\Gamma}_{\text{electrode1}}$ is connected to the ground. A resistor-based output circuit with resistance R is connected via wires between the two electrodes.

To study the vibration properties, an uniformly distributed harmonic pressure load, $P(t) = P_0 \sin(2\pi t \frac{N_{period}}{T})$, is exerted on the upper surface of the piezoelectric structure, where P_0 is the amplitude and N_{period} is the number of load cycles during the time interval $[0, T]$. The material properties of the piezoelectric structure, composed of PZT5A, are detailed in Table 5. The dimensions of the structure in the plane strain configuration are $L \times h$ in $\widehat{x}_1$ and $\widehat{x}_3$ directions. Under the plane strain assumption, the structure's thickness w in the $\widehat{x}_2$-direction is considered to be a unit thickness of 1 m. Point B $(L/2, h)$ is located at the center of the structure's upper surface and serves for result data extraction.

Eight cases are outlined in Table 6, categorized into two size groups: Size 1 and Size 2. For Size 1, with dimensions $L = 0.01\,\mathrm{m}$ and $h = 0.001\,\mathrm{m}$, six scenarios (Piezo-(1) to Piezo-(6)) vary the number of load cycles (2, 4, or 8) and resistance ($10^4\,\Omega$ or $10^{12}\,\Omega$). Size 2 cases, namely Piezo-(7) and Piezo-(8), feature larger dimensions ($L = 0.05\,\mathrm{m}$, $h = 0.01\,\mathrm{m}$) with a pressure amplitude of 550 MPa, differing in resistance to simulate circuit pass and open conditions. These cases are designed to comprehensively validate piezoelectric simulations under a range of conditions, including different sizes, pressures, numbers of periods, and resistances. Triangular mesh elements discretize the piezoelectric solid domain $\widehat{\Omega}_{sp}$ for both sizes, as shown in Figure 9. A consistent time interval $T = 4\,\mathrm{s}$ and time step $\Delta t = 0.01, \mathrm{s}$ are used across all cases for uniform comparison.

The displacement in the $\widehat{x}_3$-direction, $\widehat{\mathrm{u}}_3$, the output potential, $\widehat{\varphi}$, and charge density, Q/A, at point B are depicted in Figures 10, 11, and 12. The simulation results from our model align closely with those obtained in COMSOL for each case, considering variations in structure sizes, load amplitudes,

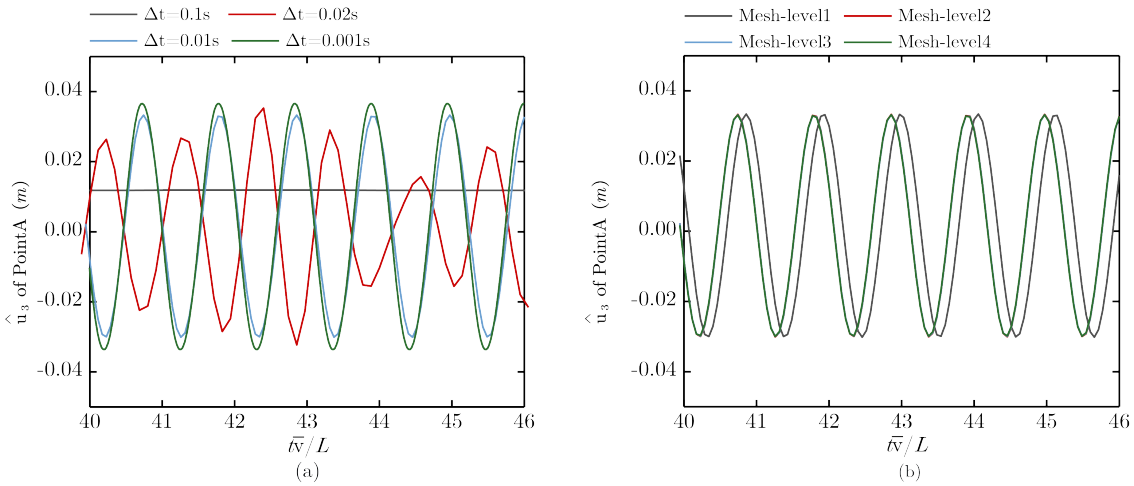

Figure 7: Displacement results of PointA in $\widehat{x}_3$ direction with (a) different time steps and (b) mesh densities.

Table 5: Material parameters for the piezoelectric structure (PZT5A)

Domain Parameters	$\widehat{\Omega}_{sp}$									
	ρ_{sp} ($\mathrm{kg/m^3}$)	c_{11} (GPa)	c_{13} (GPa)	c_{33} (GPa)	c_{44} (GPa)	e_{15} ($\mathrm{C\cdot m^{-2}}$)	e_{31} ($\mathrm{C\cdot m^{-2}}$)	e_{33} ($\mathrm{C\cdot m^{-2}}$)	ϵ_{11} ($\mathrm{C\cdot V^{-1}}$)	ϵ_{33} ($\mathrm{C\cdot V^{-1}}$)
Value	7750	120.35	75.09	110.87	21.05	12.29	-5.35	15.78	8.14×10^{-9}	7.32×10^{-9}

load cycle numbers, and circuit resistances. Due to the simplicity of the piezoelectric structure and the harmonic nature of the external load, interconnections among the three physical quantities mentioned are observed in Figures 10-12. Notably, when comparing $\widehat{\mathrm{u}}_3$ and $\widehat{\varphi}$ at Point B, for a closed circuit ($R = 10^4\,\Omega$), the temporal variation of the output potential $\widehat{\varphi}$ exhibits a quarter-phase lag relative to the displacement $\widehat{\mathrm{u}}_3$; however, in an open circuit ($R = 10^{12}\,\Omega$), the output potential $\widehat{\varphi}$ is in phase with $\widehat{\mathrm{u}}_3$. This phase behavior can be attributed to the differing conditions in closed versus open circuits, where the high resistance in an open circuit impedes the flow of charge, affecting the accumulation patterns of charge density on the electrode surface differently, as illustrated in Figure 12. In Figure 11 (a)-(f), the peak value of the output potential $\widehat{\varphi}$ increases with the number of load cycles in a closed circuit condition, attributed to a faster rate of displacement change which enhances the rate of charge accumulation, as seen in Figure 12, leading to an increase in current. However, under open circuit conditions, this phenomenon is not observed, as the accumulated charge from structure deformation is retained only on the upper electrode, without forming an effective electric current. Additionally, by comparing $\widehat{\varphi}$ and Q/A at point B, it is evident that the output potential $\widehat{\varphi}$ is directly proportional to the negative of the time derivative of Q/A. This relationship is supported by Eqs. (44-45): $\widehat{\boldsymbol{\varphi}} = -\frac{\partial Q}{\partial t} R$. Hence, when the potential $\widehat{\varphi}$ reaches a maximum, the charge density Q/A is at its minimum, and vice versa. In addition, the contours of the potential field for case Piezo-(1) at time $t = 1.00\,\mathrm{s}$ are presented in Figure 13.

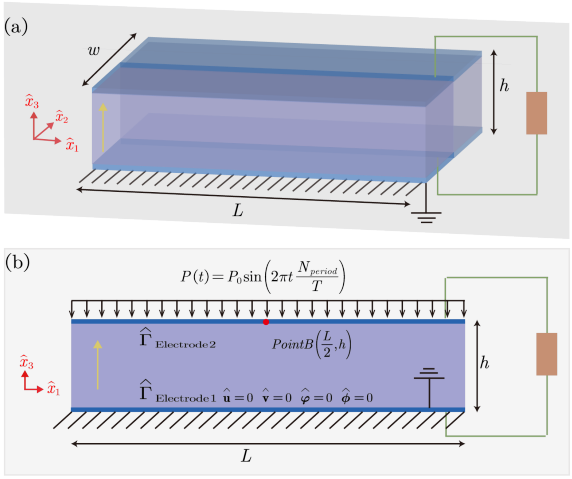

Figure 8: Geometry and boundary conditions of piezoelectric structure case: (a) 3D view (b) 2D view.

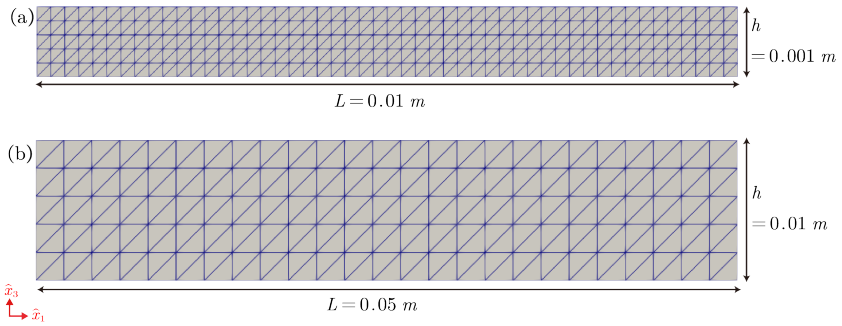

Figure 9: Meshes of piezoelectric structure cases with two sizes: (a) Size 1 (b) Size 2.

Table 6: Case configurations for piezo validation

Case name	Size (m)	P_0 (MPa)	N_{period}	$R\,(\Omega)$
Piezo-(1)	Size 1: $L = 0.01$, $h = 0.001$	4	2	10^4
Piezo-(2)				10^{12}
Piezo-(3)			4	10^4
Piezo-(4)				10^{12}
Piezo-(5)			8	10^4
Piezo-(6)				10^{12}
Piezo-(7)	Size 2: $L = 0.05$, $h = 0.01$	550	4	10^4
Piezo-(8)				10^{12}

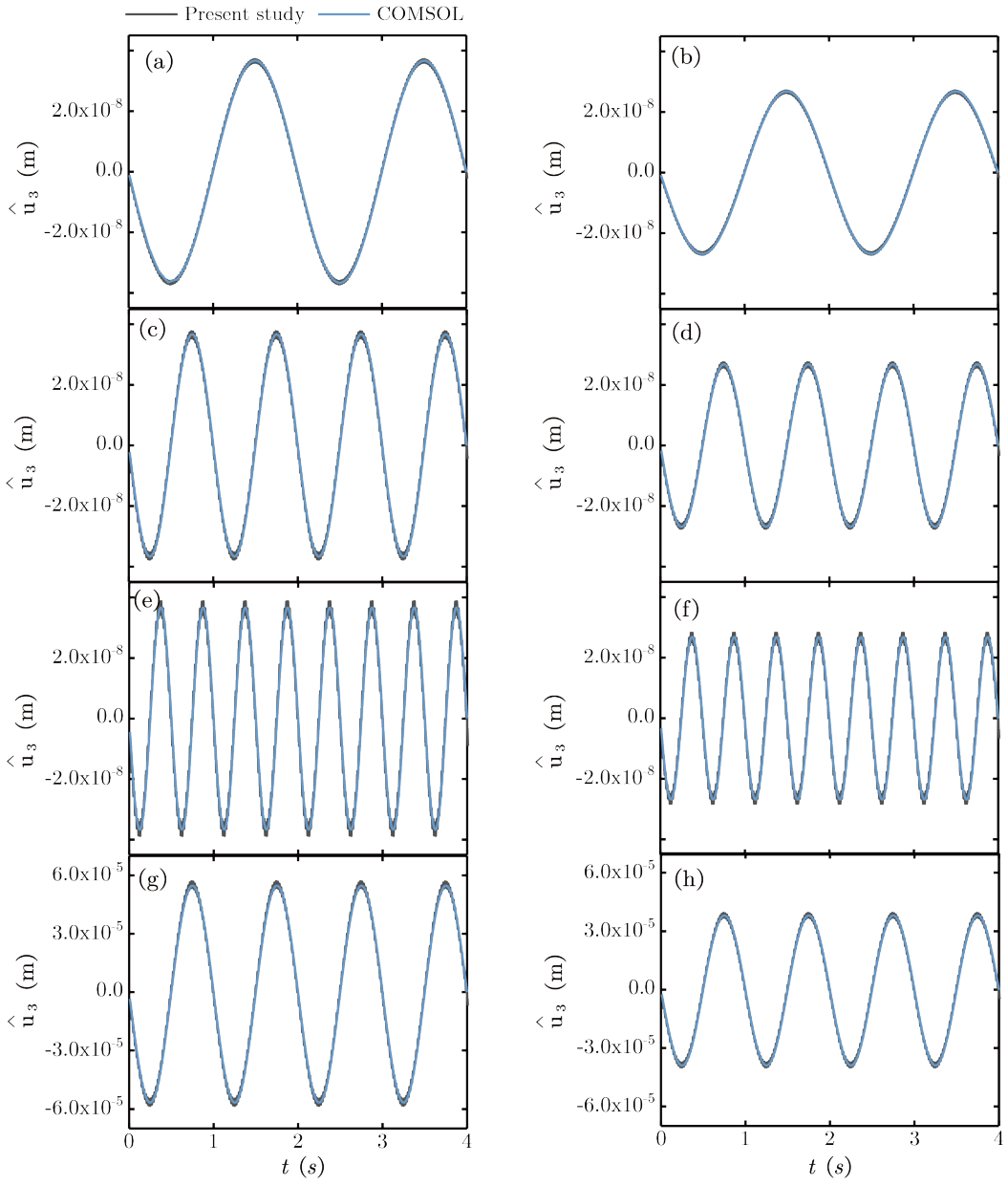

Figure 10: Displacement of Point B in $\widehat{x}_3$-direction: (a) Pizeo-(1), (b) Pizeo-(2), (c) Pizeo-(3), (d) Pizeo-(4), (e) Pizeo-(5), (f) Pizeo-(6), (g) Pizeo-(7), (h) Pizeo-(8)

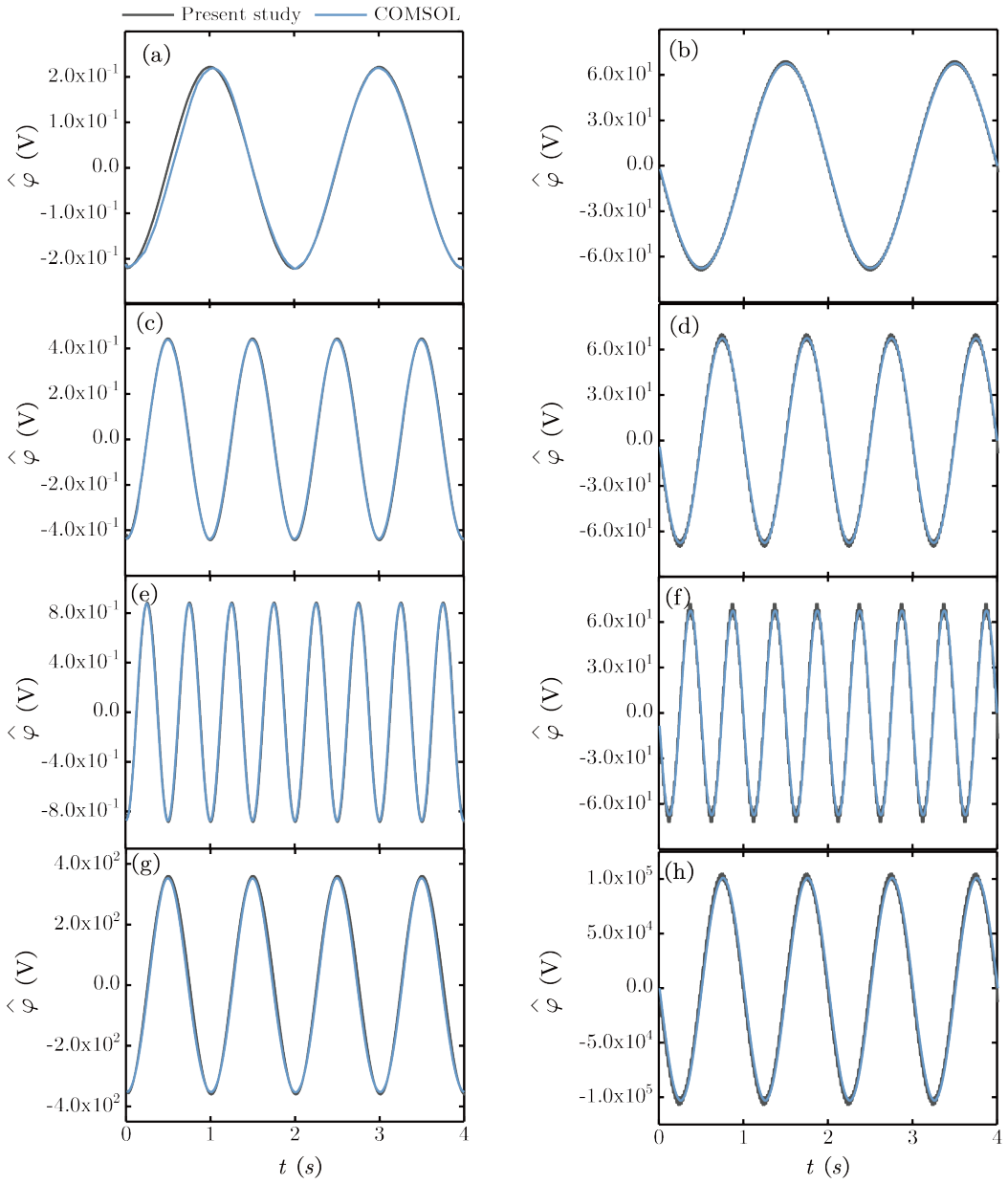

Figure 11: Potential output on electrode 2: (a) Pizeo-(1), (b) Pizeo-(2), (c) Pizeo-(3), (d) Pizeo-(4), (e) Pizeo-(5), (f) Pizeo-(6), (g) Pizeo-(7), (h) Pizeo-(8)

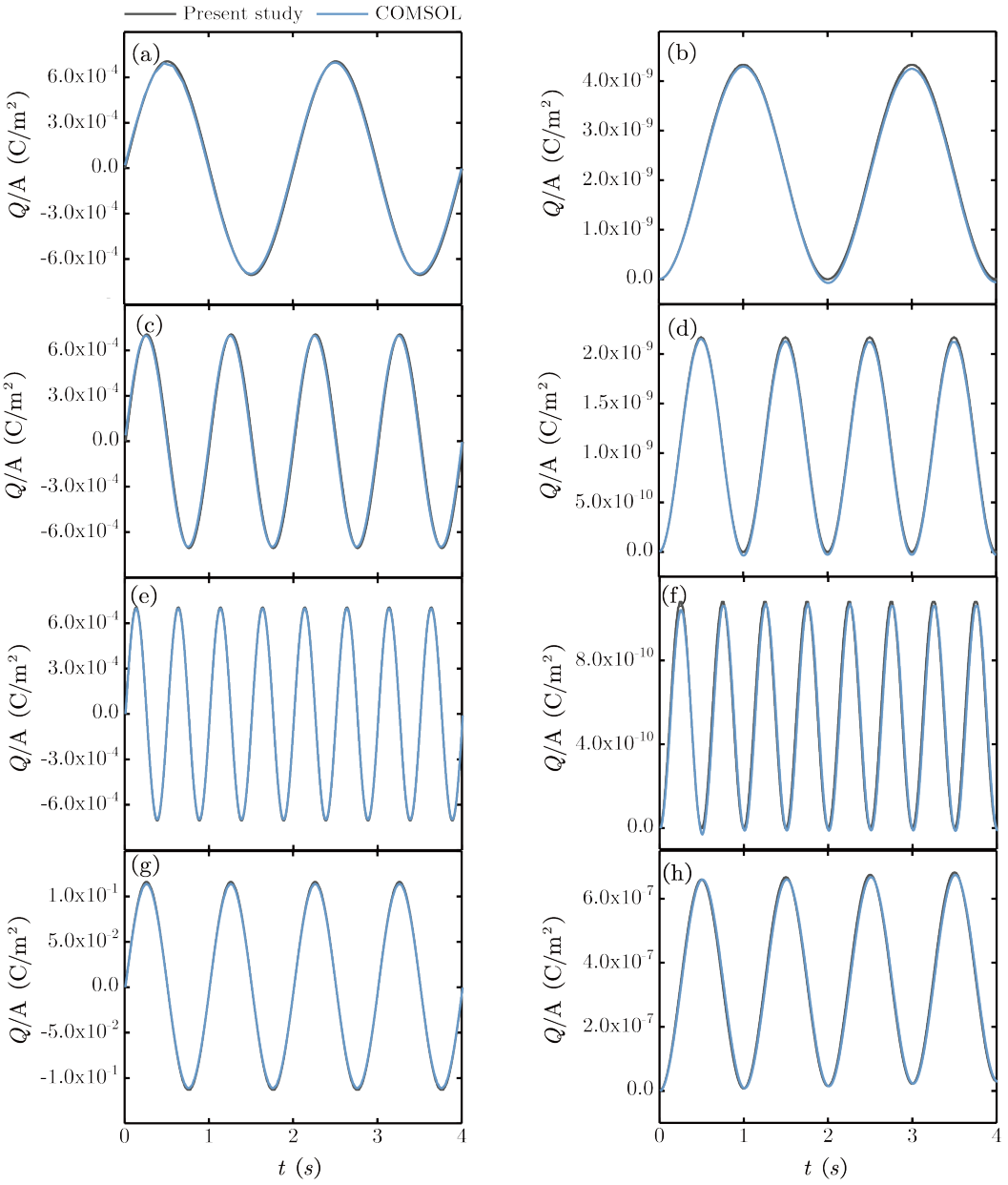

Figure 12: Electric charge density on electrode 2: (a) Pizeo-(1), (b) Pizeo-(2), (c) Pizeo-(3), (d) Pizeo-(4), (e) Pizeo-(5), (f) Pizeo-(6), (g) Pizeo-(7), (h) Pizeo-(8)

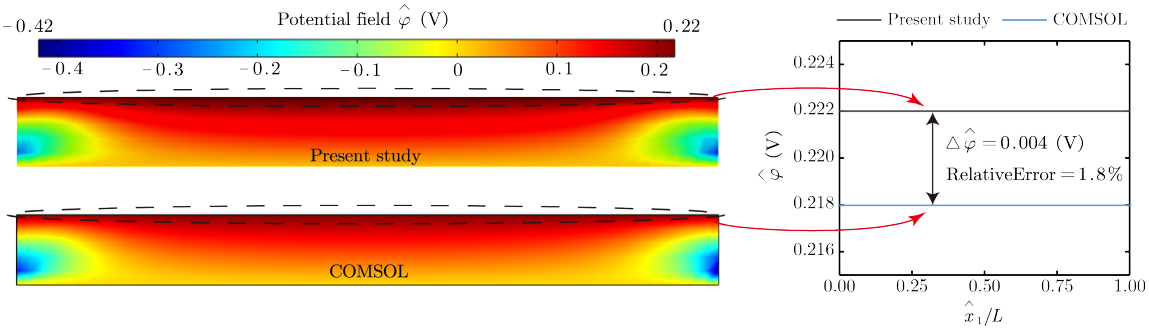

Figure 13: Potential distributions on the top surface of Case Piezo-(1) at $t = 1.00\,\mathrm{s}$

5 Integrated fluid-structure-piezoelectric interactions

After independently validating the implemented model for its ability to simulate FSI behavior in flow-induced vibrator systems and its effectiveness in modeling electromechanical coupling in piezoelectric components, this section presents several numerical cases that investigate the efficacy of the developed monolithic coupling in the integrated fluid-structure-piezoelectric coupled system with geometric nonlinearities. The model represents a PFEH system comprising a slender structure embedded with piezoelectric components, attached to a rigid bluff-body cylinder for vibration energy harvesting in fluid flow environments. To begin with, we evaluate the impact of varying the cross-sectional shapes of the base plate on vibration behavior and the consequent influence on electric energy output. Subsequently, we explore the effects of the locations and architectures of the piezoelectric components embedded in the base plate. For example, we consider piezoelectric components with inclusions, reflecting the trend towards increasingly employed architectured piezoelectric components. These cases demonstrate the advantages of full-scale finite element modeling in the design of PFEH systems, where simplified beam and plate-based models are inadequate.

5.1 Basic configuration for the reference case

All cases in Section 5 are based on a standard 2D scenario involving monolithic fluid-structure-piezoelectric coupling, as illustrated in Figure 14. We perform transient dynamic simulations to analyze energy output in a PFEH system immersed in uniform viscous fluid flow, denoted as $\widehat{\Omega}_f$. This PFEH system features a slender base structure, $\widehat{\Omega}_{ss}$, to which a piezoelectric patch, $\widehat{\Omega}_{sp}$, is attached on the upper surface. The system also includes a resistor-based output electric circuit. The base structure is connected at its left end to a rigid cylinder, which functions as a vortex generator.

Material properties for the PFEH system components are listed in Table 7. The dimensions of the fluid domain, the base plate, and the piezoelectric patch are specified as $1.6 \times 0.6\,\mathrm{m}$, $0.6 \times 0.001\,\mathrm{m}$, and $0.3 \times 0.002\,\mathrm{m}$ in the $\widehat{x}_1$ and $\widehat{x}_3$ directions, respectively. The diameter of the rigid cylinder is $0.1\,\mathrm{m}$. Electrodes are positioned at the upper and lower surfaces of the piezoelectric patch, with $\widehat{\Gamma}_{\mathrm{Electrode1}}$ connected to the ground. A wire linking the two electrodes introduces a resistor with a resistance value of $5 \times 10^4\,\Omega$. Control points for result extraction are assigned to Point A, located at the center of the right end of the base plate, and Point B, at the center of the lower surface of the piezoelectric patch $\widehat{\Gamma}_{\mathrm{Electrode1}}$. The fluid domain's inflow boundary is characterized by a uniform velocity, $\widehat{\mathrm{v}}_1 = \overline{\mathrm{v}}$, set at $2\,\mathrm{m/s}$. Symmetry boundary conditions are applied to the top and bottom sides, while a zero normal stress condition is enforced at the outflow. The surface of the circular bluff-body adheres to a no-slip boundary condition. To discretize the monolithic fluid-structure coupled system, triangular finite elements are used throughout the domains, as illustrated in Figure 15. The mesh is constructed as a unified structure, with distinct markers identifying different domains. This setup ensures that interfaces between domains share the same nodes, facilitating accurate simulations. The total number of elements in this reference case is 30198. With this foundational case established, we can proceed to the following sections by modifying the base plate's cross-sectional shape and altering the piezoelectric locations and inclusions.

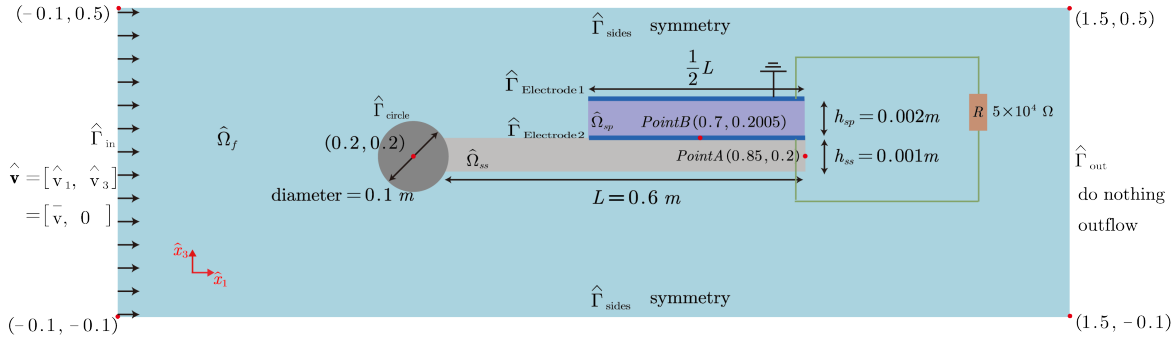

Figure 14: The fluid-structure-piezoelectric coupled system: geometry and boundary conditions.

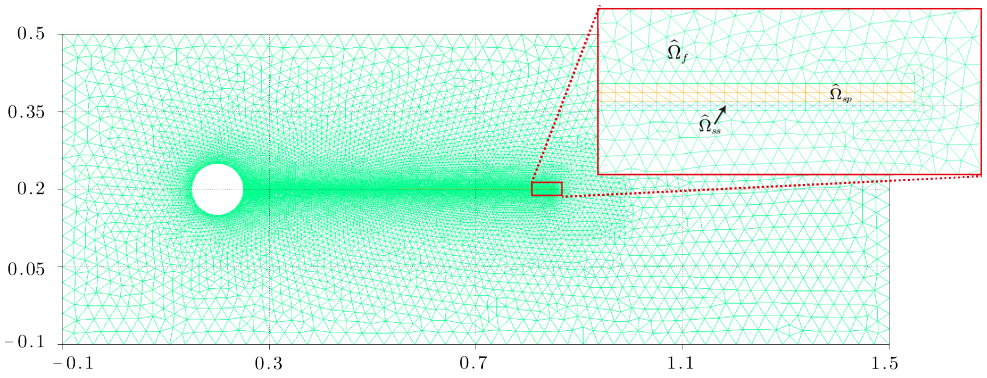

Figure 15: The fluid-structure-piezoelectric coupled system: computational mesh.

Table 7: Material composition of the coupled system

Domains	$\widehat{\Omega}_f$ (Glycerine)			$\widehat{\Omega}_{ss}$ (Aluminum alloy)			$\widehat{\Omega}_{sp}$ (PZT5A)
Parameters	ρ_f (kg/m^3)	μ_f (kg/(m · s))	$\overline{\mathrm{v}}$ (m/s)	ρ_{ss} (kg/m^3)	c_{11} GPa	c_{12} GPa	
Values	1260	1.42	2	2800	112	60.5	Listed in Table 5

5.2 Effects of base plate design on energy efficiency

Geometry design of the base plate, for example, its cross-sectional shape, is critical in determining its vibration characteristics, which in turn affects the electric energy output of the piezoelectric energy harvesting system. This influence operates through a two-fold mechanism: Firstly, the shape of the base plate determines its stiffness; Secondly, the specific geometry of the base plate modifies the local fluid flow conditions, which in turn shapes the structure's vibration. This highlights the importance of employing full-scale finite element models, as proposed in the current study, for their detailed account of the specific geometry of the structure and the interaction with the local fluid flow. Such detailed modeling is crucial, as simplified models based on beams or plates often fall short in capturing these complex dynamics.

Since the piezoelectric patch is affixed to the upper surface of the base plate, we have varied the plate's cross-sectional shape by altering the lower surface. To explore this dynamic, we modified the lower surface of the base plate, from a straight line in the standard configuration (Section 5.1) to a sinusoidal shape. This new shape is defined by the function $\text{Amplitude}\cdot\sin\left(2\pi\left(\widehat{x}_1-0.25\right)\frac{N_{\text{period}}}{L}\right)+0.2$, as illustrated in Figure 16. To assess the impact of Amplitude and N_{period}, a series of simulation cases have been established, as outlined in Table 8. Cases FSEI-(2), (3), and (6) feature amplitudes of $3/10h_{ss}$, $4/10h_{ss}$, and $5/10h_{ss}$, respectively. Additionally, Cases FSEI-(4) through (6) examine N_{period} values ranging from 2 to 6.

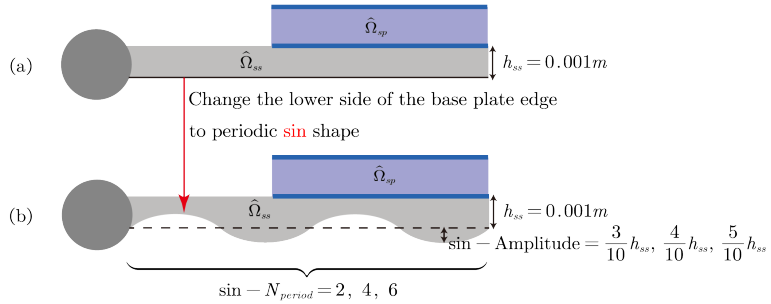

Figure 16: The sinus shape design for the base plate: (a) reference case (b) sinus based plate case

The numerical simulation results depicting vibration and energy output under various sinus shapes for the base plate are presented in Figures 17–22 and Table 9.

Case FSEI-(1) establishes a standard reference scenario for comparison with other cases that involve modifications to the base plate geometry. Figure 17 shows vorticity contours (using the Q criterion) that illustrate the generation and development of vortices within a single oscillation cycle of displacement ($\widehat{u}_3$ at Point A) in Case FSEI-(1). This visualization allows better understanding the interaction between

Table 8: Sinus shape configurations for the base plate

Case name	sin-Amplitude	sin-N_{period}
FSEI-(1)	/	/
FSEI-(2)	$3/10h_{ss}$	6
FSEI-(3)	$4/10h_{ss}$	6
FSEI-(4)	$5/10h_{ss}$	2
FSEI-(5)	$5/10h_{ss}$	4
FSEI-(6)	$5/10h_{ss}$	6

the plate and dynamic flow, where the response appears as a traveling wave with increasing amplitude from the leading edge to the trailing edge. As the tail reaches maximum displacement, strong vorticity is shed, forming discrete vortices in the wake as the tail sweeps back through the zero displacement point. This symmetrical process results in cyclic variation in electrical energy output.

Influence of the sinus shape amplitude has been explored. In Figure 18, the transient history of displacement at Point A, the full-body lift coefficient, output potential, and power of the piezoelectric patch are observed with varying sinus amplitudes. These physical quantities exhibit synchronized variations, and as the sinus amplitude increases, they take longer to achieve periodic cycle fluctuations, indicating a decrease in oscillation frequencies f, as outlined in Table 9. This decrease is attributable to the sinus shape of the plate cross-section causing a shift in the overall mass distribution of the base plate towards the free end, therefore reducing the resonant frequency of the structure [43]. The phase plots in 20 (a)-(c), (f) show that phases spiral to a typical limit cycle trajectory (LCO) under all conditions. Although an increase in sinus amplitude enhances the base plate vibration amplitude, this is primarily observed in the front half of the base plate and not in the second half that controls the deformation of the piezoelectric patch.

To evaluate the energy harvesting efficiency of the fluid-structure-piezoelectric coupled system, we employ the classical definition used for wind turbines. This definition calculates efficiency as the ratio of the mean power output to the mean kinetic energy flux passing through the section occupied by the device within the flow [44]. This leads to the expression: efficiency $= \frac{\text{AveragedPower}}{0.5\rho\bar{\text{v}}^3(2\widehat{\text{u}}_{3,\max})}$. Observations indicate a decrease in averaged output powers and an increase in $\widehat{\text{u}}_{3,\max}$ with rising sinusoidal shape amplitudes, suggesting a reduction in energy harvesting efficiency, as detailed in Table 9.

We next consider the influence of the sinus shape period number, N_{period}. Figure 19 displays the transient history of displacement at Point A, the full-body lift coefficient, potential, and power of the piezoelectric patch with varying N_{period}. The transient responses with a smaller $N_{\text{period}} = 2$ coincide with those of the reference case ref-FSEI(1). However, results for larger $N_{\text{period}} = 4, 6$ show a closer resemblance due to the steeper cross-sectional shape gradient of the base plate induced by a larger N_{period}, although the effects of the shape do not continue to intensify beyond this point. Comparatively, the sinus shape period number enhances power output more effectively than the sinus shape amplitude. However, larger N_{period} values are not necessarily advantageous; when $N_{\text{period}} = 4$ (case FSEI-(5)), the peak power reaches a maximum of 1.72 W, which is 2.42 times that of case ref-FSEI-(1)), as depicted in Figure 22. In this instance, the vortex formation is significantly stronger in case FSEI-(5) compared to the other cases at the same response state. Despite reaching this peak, case FSEI-(5) cannot sustain high power levels for an extended period; thus, case FSEI-(4) achieves the highest average power. Furthermore, case FSEI-(4) also shows the smallest free-end displacement, as illustrated in Figure 21. Consequently, by the established metrics, FSEI-(4) maintains the highest system efficiency, as indicated in Table 9

Despite the weak base plate thickness 0.001 m, cases FSEI-(1) to (6) demonstrate that modifications to the base plate geometry significantly influence the vibration response and the energy output efficiency.

Table 9: Statistic data for cases with different sin shapes.

Case name	f (Hz)	$\widehat{u}_{3,\max}/L$	Averaged Power (W)	Efficiency (%)
ref-FSEI-(1)	2.00	0.167	0.225	0.0223
FSEI-(2)	1.96	0.185	0.191	0.0171
FSEI-(3)	1.92	0.207	0.170	0.0136
FSEI-(4)	2.13	0.140	0.234	0.0276
FSEI-(5)	1.89	0.217	0.183	0.0139
FSEI-(6)	1.89	0.217	0.139	0.0106

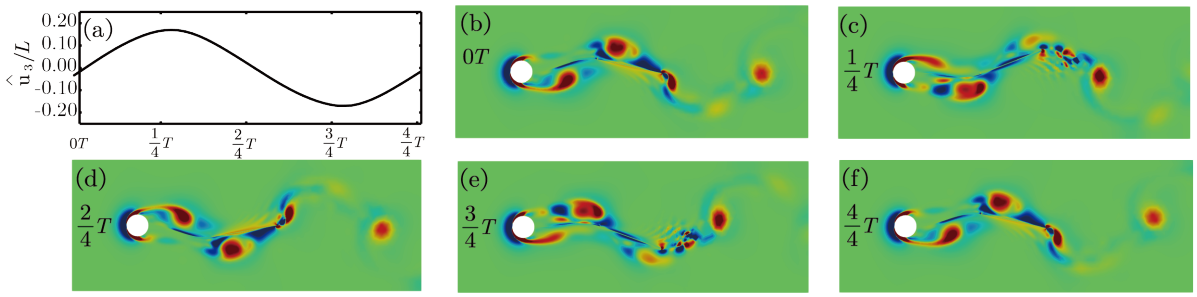

Figure 17: Vortex shedding development within a single oscillation period for case FSEI-(1)

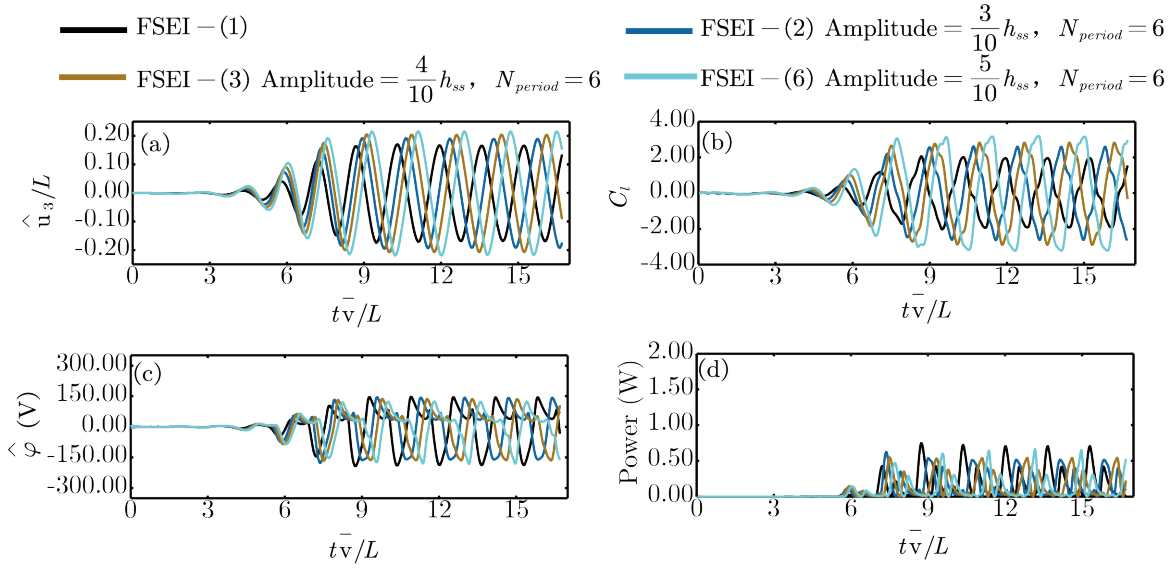

Figure 18: Time history of (a) displacement $\widehat{u}_3$ of Point A in $\widehat{x}_3$ direction, (b) lift force coefficient of the full structure body (including the rigid part), (c) the potential $\widehat{\psi}$ of Point B, (d) the power of the output circuit (including cases FSEI-(1), FSEI-(2), FSEI-(3), FSEI-(6))

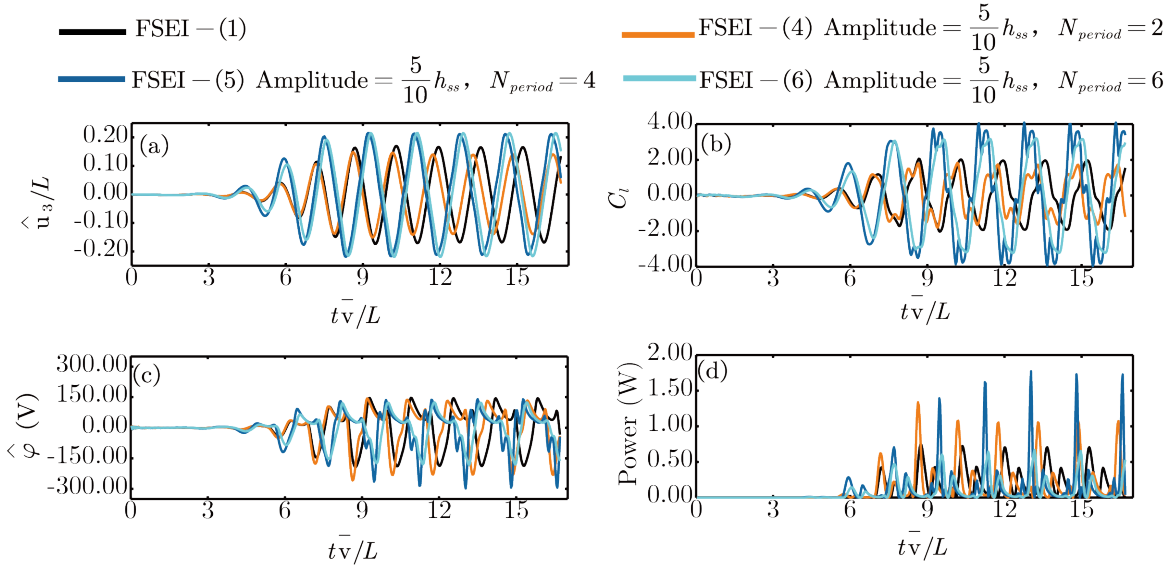

Figure 19: Time history of (a) displacement $\hat{u}_3$ of Point A in $\hat{x}_3$ direction, (b) lift force coefficient of the full structure body (including the rigid part), (c) the potential $\hat{\psi}$ of Point B, (d) the power of the output circuit (including cases FSEI-(1), FSEI-(4), FSEI-(5), FSEI-(6))

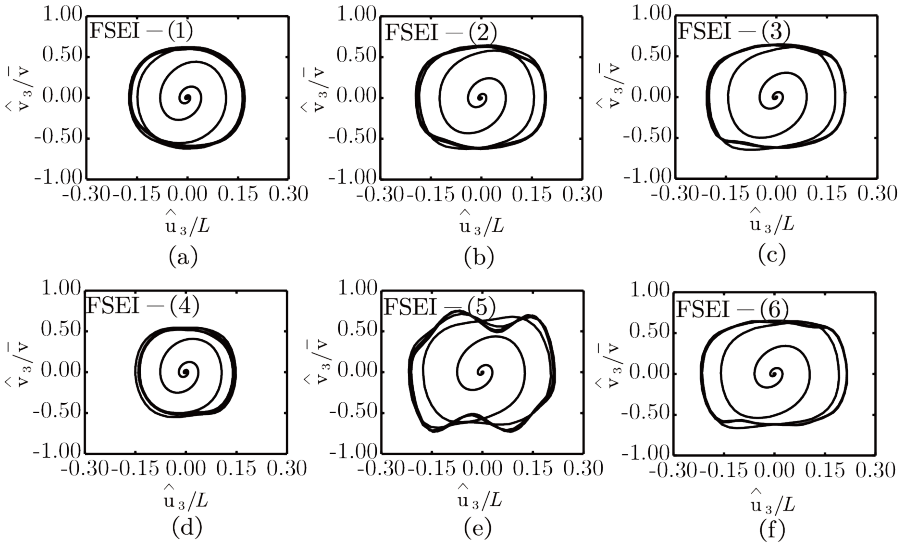

Figure 20: The phase plane trajectories for cases FSEI-(1) to (6)

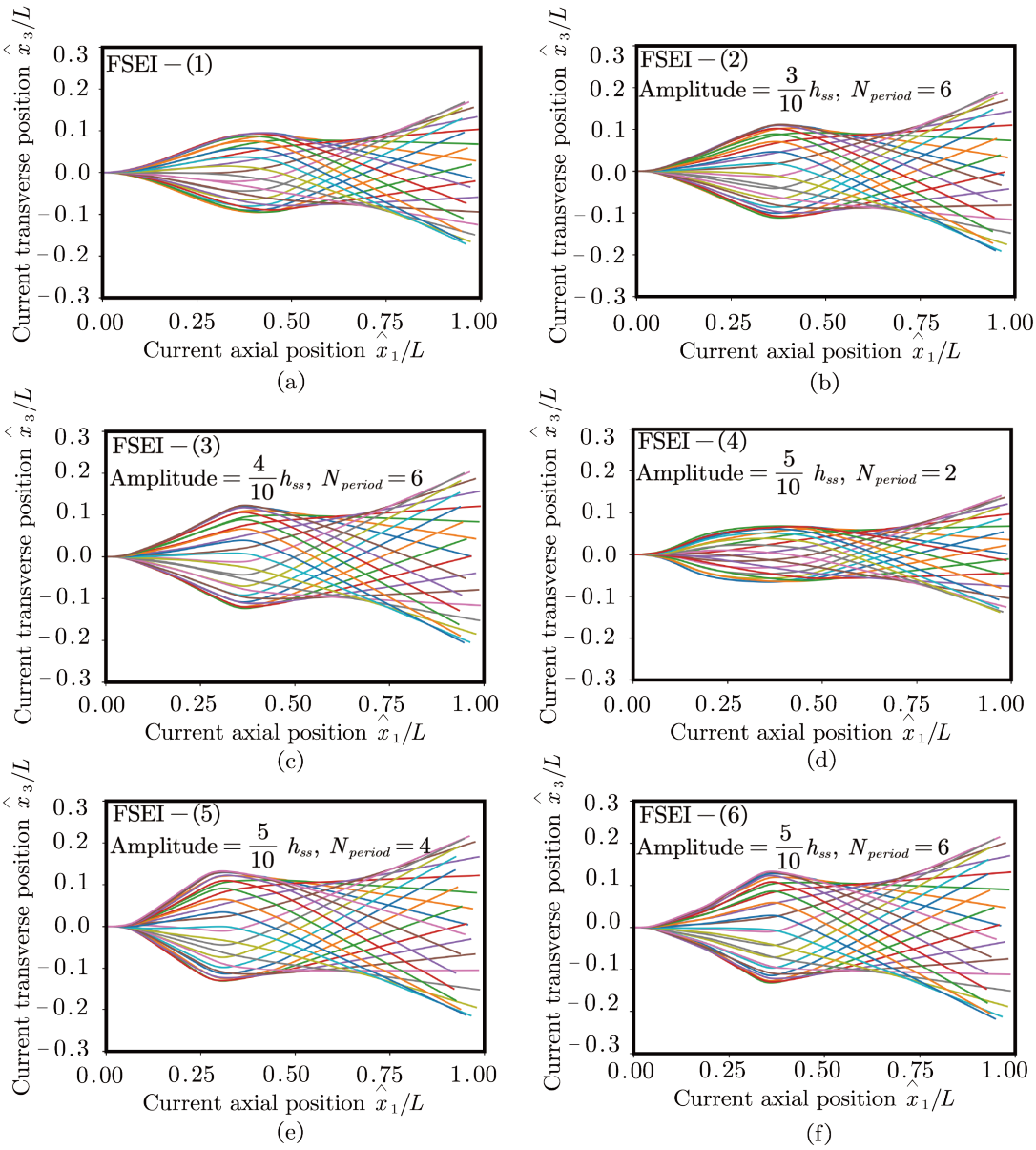

Figure 21: Full-body response of the base plate over a complete oscillation cycle for cases FSEI-(1) to (6)

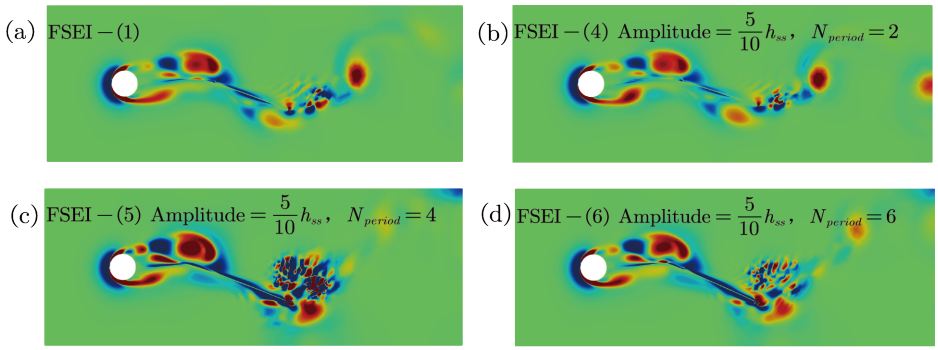

Figure 22: Vorticity of cases with different sin shape N_{period} at the same state when the free end of the base plate reaches its biggest displacement: (a) FSEI-(1), (b) FSEI-(4), (c) FSEI-(5), (d) FSEI-(6)

5.3 Effects of piezoelectric patch implementation: location and architecture

In addition to the base plate geometry, the design and implementation technique of the piezoelectric patch are important in shaping the energy output behavior of PFEH systems. Recent emergence of architected piezoelectric sensors, particularly those using composite materials, further amplifies this point. These sensors employ structured material designs to enhance performance and functionality, posing modeling challenges for simplified beam or plate models which typically consider homogenized behaviors. However, factors such as patch thickness, which is often non-negligible, and placement location lead to complex fluid-structure interactions. These interactions are inadequately represented by geometrically simplified models but can be accurately captured by full-scale models like the one used in this study. This section explores various scenarios involving composite piezoelectric components implemented at different locations within the system. We aim to assess their impact on energy output efficiency, taking into account the associated FSI effects. This exploration motivates the current test cases using full-scale models to optimize PFEH systems.

In this section, we use case FSEI-(1) as the reference to explore the effects of varying the position of the piezoelectric patch along the base plate. The patch is moved from the free end towards the fixed end of the base plate, as shown in Figure 23(b). The distance from the right edge of the piezoelectric patch to the free end of the base plate, denoted as δL, is systematically varied with values of $0/8L$, $1/8L$, $2/8L$, and $3/8L$. Additionally, to illustrate the capability of our model to capture the internal structural design of the piezoelectric component, we present a demonstration case depicted in Figure 23(c). In this case, an inclusion made of aluminium alloy, the same material used in $\widehat{\Omega}_{ss}$, representing half the volume of $\widehat{\Omega}_{sp}$, has been implemented . Details of the studied cases are listed in Table 10.

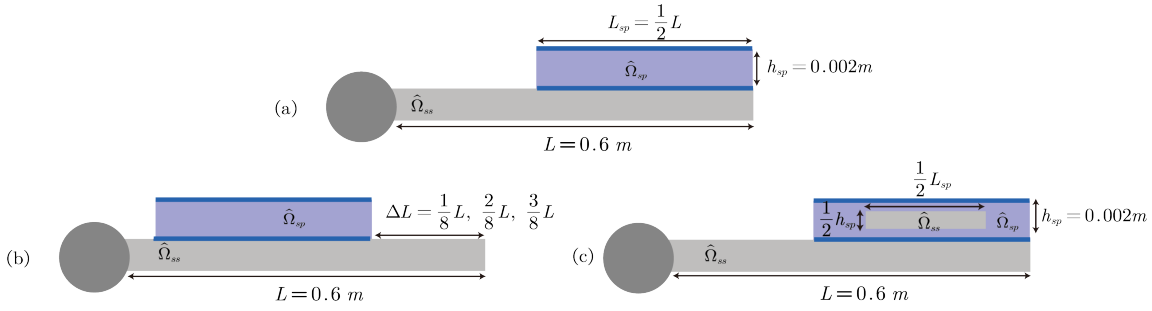

Figure 23: Schematic diagram of position change and internal inclusion of piezoelectric patch: (a) reference case (b) with different locations (c) with a inclusion

The numerical simulation results illustrating the vibration and energy output with varying piezoelectric patch locations and inclusions are presented in Figures 24-28 and Table 11.

Table 10: Piezoelectric patch configurations

Case name	$\Delta L/L$	with inclusion in $\widehat{\Omega}_{sp}$
FSEI-(1)	0	no
FSEI-(7)	1/8	no
FSEI-(8)	2/8	no
FSEI-(9)	3/8	no
FSEI-(10)	0	yes

Table 11: Statistics of the cases with different piezoelectric patch designs.

Case name	f (Hz)	$\widehat{\mathrm{u}}_{3,\max}/L$	Averaged Power (W)	Efficiency (%)
ref-FSEI-(1)	2.00	0.167	0.225	0.0223
FSEI-(7)	2.33	0.108	0.444	0.0678
FSEI-(8)	2.50	0.038	0.204	0.0882
FSEI-(9)	3.70	0.038	0.032	0.0133
FSEI-(10)	2.17	0.142	0.104	0.0121

The time-domain results shown in Figure 24 clearly demonstrate that the location of the piezoelectric patch has significant impact on both the dynamic response and electrical energy output, exerting a greater influence than the shape modifications to the base plate discussed in Section 5.2. As the piezoelectric patch is moved towards the fixed end of the base plate, the displacement amplitude at the free end decreases, while the vibration frequency increases. Of the four tested locations, the instantaneous potential amplitude is highest at $\Delta L = 1/8L$, where the instantaneous power is 2.14 times that of case FSEI-(1). The statistical analysis from Table 11 indicates that while the coupling system produces the highest average output power at $\Delta L = 1/8L$, the maximum energy conversion efficiency is observed at $\Delta L = 2/8L$. This increased efficiency is attributed to the relatively smaller displacement amplitude at the free end for case FSEI-(8) at $\Delta L = 2/8L$, which compensates for the decrease in average power.

The phase plane trajectories depicted in Figure 26 reveal that shifting the location of the piezoelectric patch does not prevent the coupled system from eventually stabilizing into a limit cycle oscillation state after a certain period. However, as ΔL increases, the range of the phase plot diminishes. Additionally, the full-body response shown in Figure 27 exhibits a noticeable reduction in the vibration range of the entire plate structure with increasing ΔL. This reduction can be attributed to two factors: the transfer of mass from the free end to the fixed end, and an increase in structural stiffness near the fixed end, which collectively hinder the plate's ability to generate larger oscillations. Furthermore, the vorticity plots in Figure 28 display a significant decrease in vorticity intensity as the plate becomes more rigid and less prone to significant vibrations. This reduction directly affects the intensity of vortices attached to the plate. These observations are crucial for optimizing the placement of the piezoelectric element to enhance the electrical energy output efficiency of the system.

In case FSEI-(10), where the piezoelectric component contains an inclusion of aluminium alloy, the mass near the free end of the plate is reduced due to the lower density of aluminium alloy compared to the piezoelectric material. This modification leads to a decrease in the amplitude of displacement and an increase in the vibration frequency near the free end, as illustrated in Figure 25. Consequently, with implementation of the aluminium inclusion, the electricity output of the coupled system is reduced. The instantaneous power is lower than that of the reference case, and the averaged power has decreased by nearly 53% compared to the reference case, as shown in Table 11.

It is important to emphasize that the current scenario does not aim to propose a specific and effective design for piezoelectric structures. Rather, it highlights the potential of our model, particularly in accommodating the design of PFEH systems that involve structured components and requirements for complex fluid-structure interactions.

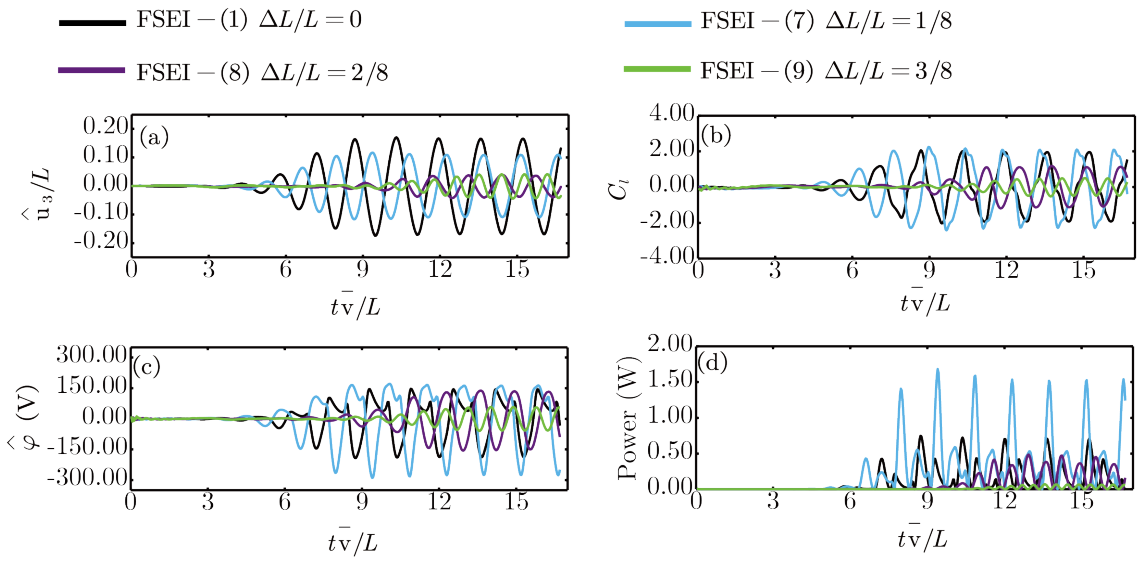

Figure 24: Time history of (a) displacement $\widehat{u}_3$ of Point A in $\widehat{x}_3$ direction, (b) lift force coefficient of the full structure body (including the rigid part), (c) the potential $\widehat{\psi}$ of Point B, (d) the power output (including cases FSEI-(1), FSEI-(7), FSEI-(8), FSEI-(9))

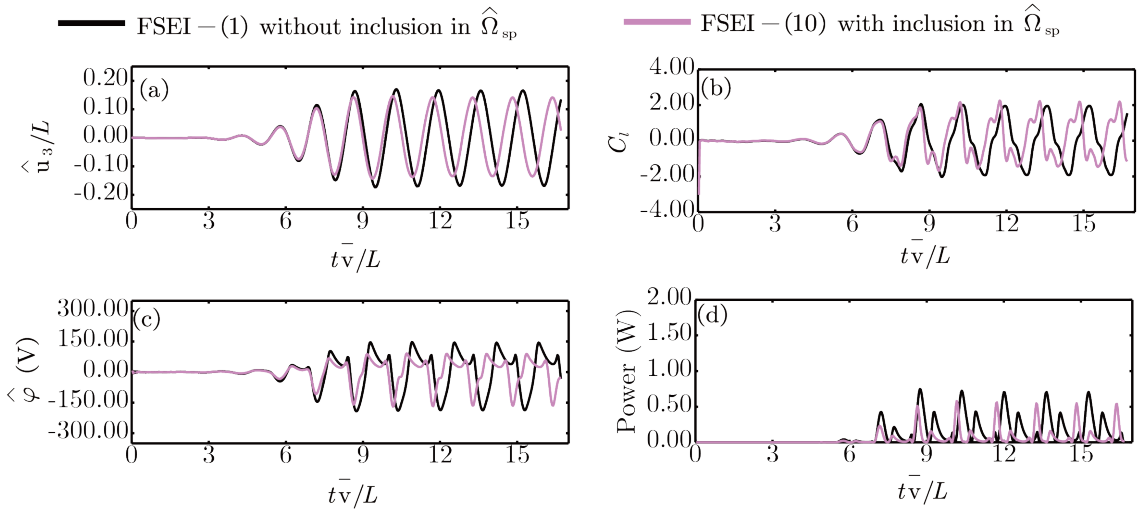

Figure 25: Time history of (a) displacement $\widehat{u}_3$ of Point A in $\widehat{x}_3$ direction, (b) lift force coefficient of the full structure body (including the rigid part), (c) the potential $\widehat{\psi}$ of Point B, (d) the power output (including cases FSEI-(1), FSEI-(10))

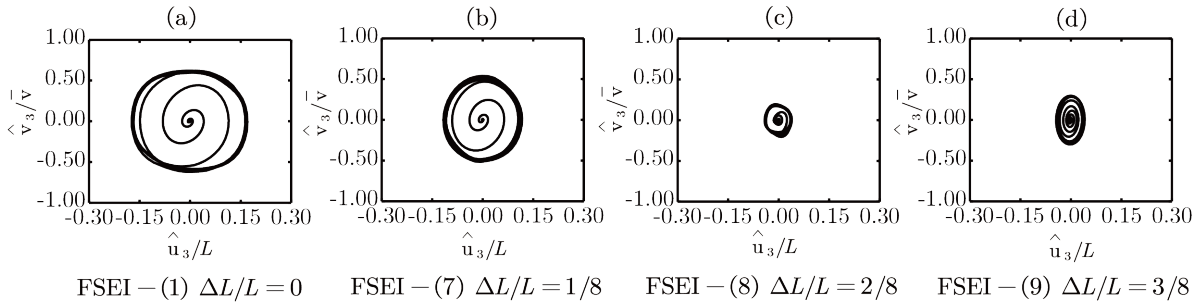

Figure 26: The phase plane trajectories for cases FSEI-(1) and FSEI-(7) to (9)

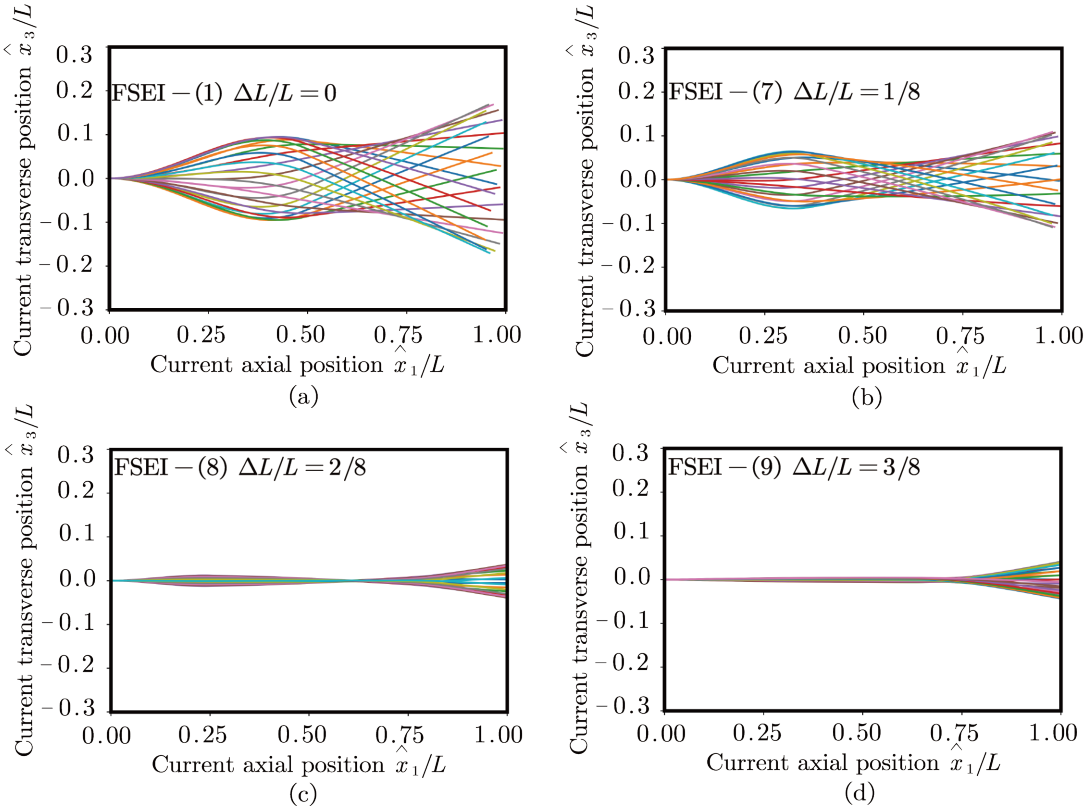

Figure 27: Full-body response of the base plate over a complete oscillation cycle for cases FSEI-(1) and FSEI-(7) to (9)

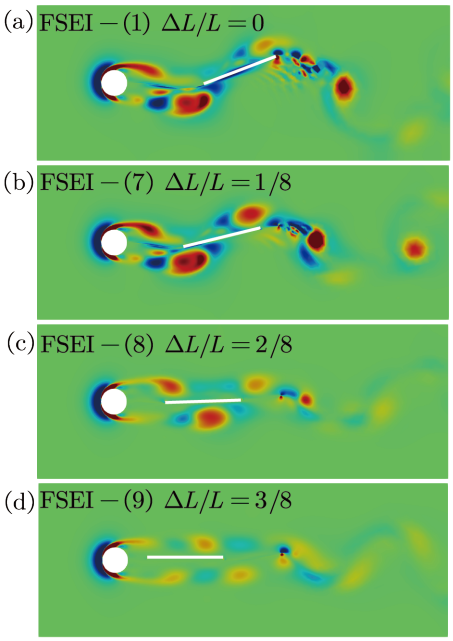

Figure 28: Vorticity of cases with different sin shape N_{period} at the same state when the free end of the base plate reaches its biggest displacement: (a) FSEI-(1), (b) FSEI-(4), (c) FSEI-(5), (d) FSEI-(6)

6 Conclusion

This study introduces a full-scale finite element model featuring geometric nonlinearities and based on a monolithic coupling approach for the design and simulation of thin-walled piezoelectric fluid energy harvesters (PFEH). Operating within steady or transient fluid environments, these systems require complex fluid-structure-piezoelectric interactions. The proposed model, implemented within the FEniCS environment and extending its TurtleFSI library, addresses several challenges including the incorporation of piezoelectric materials, the integration of output electric circuits, and the management of electromechanical boundary conditions. For the last point, penalty functions have been used to achieve uniform electric potentials at electrode surfaces. The development process has been rigorously validated against literature benchmarks and commercial software outputs, confirming the effectiveness of our approach.

To demonstrate the utility of the model in PFEH design, we explored geometric variations in the base plate and the piezoelectric patch through a series of test cases. The results reveal that even minor modifications, such as changing the cross-sectional shape of the base plate or adjusting the location and internal composition of the piezoelectric patch, significantly influence the system's vibrational behavior and subsequently the energy harvesting efficiency. Furthermore, the current emergence of architected piezoelectric sensors, especially those using composite materials, has added complexities that underline the necessity of our modeling approach. These observations highlight the role of precise, full-scale finite element modeling in capturing complex fluid-structure interactions, a task that simplified beam or plate models struggle with.

However, it is important to recognize the limitations of this methodology. The extensive mesh requirements for accurate fluid and structure interaction simulation pose significant computational demands, especially in large-scale applications with complex geometries. Moreover, the monolithic solution scheme may face challenges at high Reynolds numbers, indicating the potential need to integrate turbulence models to enhance its applicability. Looking forward, future work will aim to extend this modeling approach to 3-dimensional problems. Such an expansion is important for the more detailed design of piezoelectric structures and their microstructures. Moving to a 3-dimensional framework will not only broaden the model's applicability but also enable a deeper exploration of the intricate dynamics inherent in advanced piezoelectric energy systems.

Acknowledgments

This work was supported by the China Scholarship Council (CSC No. 202106050012).

Appendix A

The linear elasticity matrix for the base plate material $\widehat{\Omega}_{ss}$, based on the plane strain assumption in two-dimensional problems employed in this study, is expressed in the following form:

$$[\mathbf{C}_{ss}] = \begin{bmatrix} c_{11} & c_{12} & 0 \\ c_{12} & c_{11} & 0 \\ 0 & 0 & \frac{c_{11}-c_{12}}{2} \end{bmatrix}, \tag{70}$$

where the parameters c_{11} and c_{12} are specific to the material selected for the base plate.

Appendix B

The linear elasticity matrix for the piezoelectric material $\widehat{\Omega}_{sp}$, based on the plane strain assumption in two-dimensional problems used in this study, is expressed in the following form:

$$[\mathbf{C}_{sp}] = \begin{bmatrix} c_{11} & c_{13} & 0 \\ c_{13} & c_{33} & 0 \\ 0 & 0 & c_{44} \end{bmatrix} , \tag{71}$$

where the piezoelectric materials are typically transversely isotropic, meaning the terms in $[\mathbf{C}_{sp}]$ differ from those in $[\mathbf{C}_{ss}]$.

Additionally, the piezoelectric coupling matrix and the dielectric permittivity matrix are expressed as follows:

$$[\mathbf{e}_{sp}] = \begin{bmatrix} 0 & e_{31} \\ 0 & e_{33} \\ e_{15} & 0 \end{bmatrix} , \tag{72}$$

$$[\boldsymbol{\epsilon}_{sp}] = \begin{bmatrix} \epsilon_{11} & 0 \\ 0 & \epsilon_{33} \end{bmatrix} , \tag{73}$$

The parameters within these matrices are specific to the piezoelectric material selected for the piezoelectric patch.

References

[1] S. Madakam, R. Ramaswamy, and S. Tripathi. Internet of things (iot): A literature review. Journal of Computer and Communications, 03(05):164–173, 2015.

[2] X. Yan, G. Li, Z. Wang, Z. Yu, K. Wang, and Y. Wu. Recent progress on piezoelectric materials for renewable energy conversion. Nano Energy, 77:105180, November 2020.

[3] A. Naqvi, A. Ali, W. A. Altabey, and S. A. Kouritem. Energy harvesting from fluid flow using piezoelectric materials: A review. Energies, 15(19):7424, October 2022.

[4] M. Hamlehdar, A. Kasaeian, and M. R. Safaei. Energy harvesting from fluid flow using piezoelectrics: A critical review. Renewable Energy, 143:1826–1838, December 2019.

[5] H. D. Akaydin, N. Elvin, and Y. Andreopoulos. The performance of a self-excited fluidic energy harvester. Smart Materials and Structures, 21(2):025007, January 2012.

[6] J. Prinzie, F. M. Simanjuntak, P. Leroux, and T. Prodromakis. Low-power electronic technologies for harsh radiation environments. Nature Electronics, 4(4):243–253, April 2021.

[7] S. Kaneko, G. Hong, N. Mitsume, T. Yamada, and S. Yoshimura. Numerical study of active control by piezoelectric materials for fluid–structure interaction problems. Journal of Sound and Vibration, 435:23–35, November 2018.

[8] C. Covaci and A. Gontean. Piezoelectric energy harvesting solutions: A review. Sensors, 20(12):3512, June 2020.

[9] R. Li, Y. Yu, B. Zhou, Q. Guo, M. Li, and J. Pei. Harvesting energy from pavement based on piezoelectric effects: Fabrication and electric properties of piezoelectric vibrator. Journal of Renewable and Sustainable Energy, 10(5), September 2018.

[10] H. Elahi, M. Eugeni, and P. Gaudenzi. A review on mechanisms for piezoelectric-based energy harvesters. Energies, 11(7):1850, July 2018.

[11] M. Bucelli, L. Dede, A. Q. null, and C. Vergara. Partitioned and monolithic algorithms for the numerical solution of cardiac fluid-structure interaction. Communications in Computational Physics, 32(5):1217–1256, June 2022.

[12] J. Degroote, K.-J. Bathe, and J. Vierendeels. Performance of a new partitioned procedure versus a monolithic procedure in fluid–structure interaction. Computers and Structures, 87(11–12):793–801, June 2009.

[13] J. A. González and K. Park. Three-field partitioned analysis of fluid–structure interaction problems with a consistent interface model. Computer Methods in Applied Mechanics and Engineering, 414:116134, September 2023.

[14] C. Wood, A. J. Gil, O. Hassan, and J. Bonet. A partitioned coupling approach for dynamic fluid–structure interaction with applications to biological membranes. International Journal for Numerical Methods in Fluids, 57(5):555–581, May 2008.

[15] R. Zwaan and B. Prananta. Fluid/structure interaction in numerical aeroelastic simulation. International Journal of Non-Linear Mechanics, 37(4–5):987–1002, June 2002.

[16] W. Lim and R. Xiao. Fluid-structure interaction analysis of gravity-based structure (gbs) offshore platform with partitioned coupling method. Ocean Engineering, 114:1–9, March 2016.

[17] U. Langer and H. Yang. Robust and efficient monolithic fluid-structure-interaction solvers. International Journal for Numerical Methods in Engineering, 108(4):303–325, February 2016.

[18] T. Wick. Adaptive finite element simulation of fluid-structure interaction with application to heart-valve dynamics. 2012.

[19] S. Turek and J. Hron. Proposal for Numerical Benchmarking of Fluid-Structure Interaction between an Elastic Object and Laminar Incompressible Flow, page 371–385. Springer Berlin Heidelberg.

[20] A. Zilian and A. Legay. The enriched space–time finite element method (est) for simultaneous solution of fluid–structure interaction. International Journal for Numerical Methods in Engineering, 75(3):305–334, December 2007.

[21] C. S. Peskin and D. M. McQueen. A three-dimensional computational method for blood flow in the heart i. immersed elastic fibers in a viscous incompressible fluid. Journal of Computational Physics, 81(2):372–405, April 1989.

[22] L. Shang, C. Hoareau, and A. Zilian. Modeling and simulation of thin-walled piezoelectric energy harvesters immersed in flow using monolithic fluid–structure interaction. Finite Elements in Analysis and Design, 206:103761, September 2022.

[23] S. Chawdhury and G. Morgenthal. A partitioned solver to simulate large-displacement fluid–structure interaction of thin plate systems for vibration energy harvesting. Computers and Structures, 224:106110, November 2019.

[24] O. Doaré and S. Michelin. Piezoelectric coupling in energy-harvesting fluttering flexible plates: linear stability analysis and conversion efficiency. Journal of Fluids and Structures, 27(8):1357–1375, November 2011.

[25] S. Kaneko and S. Yoshimura. Coupled analysis for active control and energy harvesting from flow-induced vibration. Journal of Advanced Simulation in Science and Engineering, 9(1):1–19, 2022.

[26] Q. Lu, L. Liu, F. Scarpa, J. Leng, and Y. Liu. A novel composite multi-layer piezoelectric energy harvester. Composite Structures, 201:121–130, October 2018.

[27] S. Lee and B. D. Youn. A new piezoelectric energy harvesting design concept: multimodal energy harvesting skin. IEEE Transactions on Ultrasonics, Ferroelectrics, and Frequency Control, 58(3):629–645, March 2011.

[28] Y. Jeon, R. Sood, J.-h. Jeong, and S.-G. Kim. Mems power generator with transverse mode thin film pzt. Sensors and Actuators A: Physical, 122(1):16–22, July 2005.

[29] S. Ravi and A. Zilian. Simultaneous finite element analysis of circuit-integrated piezoelectric energy harvesting from fluid-structure interaction. Mechanical Systems and Signal Processing, 114:259–274, January 2019.

[30] B. Seyed-Aghazadeh, H. Samandari, and S. Dulac. Flow-induced vibration of inherently nonlinear structures with applications in energy harvesting. Physics of Fluids, 32(7), July 2020.

[31] Automated Solution of Differential Equations by the Finite Element Method: The FEniCS Book. Springer Berlin Heidelberg, 2012.

[32] B. T. Helenbrook. Mesh deformation using the biharmonic operator. International Journal for Numerical Methods in Engineering, 56(7):1007–1021, 2003.

[33] T. Dunne. Adaptive finite element approximation of fluid-structure interaction based on eulerian and arbitrary lagrangian-eulerian variational formulations. Dissertation, 2007.

[34] T. Richter and T. Wick. Finite elements for fluid–structure interaction in ale and fully eulerian coordinates. Computer Methods in Applied Mechanics and Engineering, 199(41–44):2633–2642, October 2010.

[35] P. Sackinger, P. Schunk, and R. Rao. A newton–raphson pseudo-solid domain mapping technique for free and moving boundary problems: A finite element implementation. Journal of Computational Physics, 125(1):83–103, April 1996.

[36] K. Stein, T. Tezduyar, and R. Benney. Mesh moving techniques for fluid-structure interactions with large displacements. Journal of Applied Mechanics, 70(1):58–63, January 2003.

[37] A. Shamanskiy and B. Simeon. Mesh moving techniques in fluid-structure interaction: robustness, accumulated distortion and computational efficiency. Computational Mechanics, 67(2):583–600, December 2020.

[38] T. Wick. Fluid-structure interactions using different mesh motion techniques. Computers and Structures, 89(13–14):1456–1467, July 2011.

[39] J. Hron and S. Turek. A Monolithic FEM/Multigrid Solver for an ALE Formulation of Fluid-Structure Interaction with Applications in Biomechanics, page 146–170. Springer Berlin Heidelberg, 2006.

[40] C. Multiphysics. Introduction to comsol multiphysics. COMSOL Multiphysics, (9(2018)):32, February 1998.

[41] A. Bergersen, A. Slyngstad, S. Gjertsen, A. Souche, and K. Valen-Sendstad. turtlefsi: A robust and monolithic fenics-based fluid-structure interaction solver. Journal of Open Source Software, 5(50):2089, June 2020.

[42] S. Turek, J. Hron, M. Razzaq, H. Wobker, and M. Schäfer. Numerical Benchmarking of Fluid-Structure Interaction: A Comparison of Different Discretization and Solution Approaches, page 413–424. Springer Berlin Heidelberg, July 2010.

[43] H. Li, C. Tian, and Z. D. Deng. Energy harvesting from low frequency applications using piezoelectric materials. Applied Physics Reviews, 1(4):041301, December 2014.

[44] S. Michelin and O. Doaré. Energy harvesting efficiency of piezoelectric flags in axial flows. Journal of Fluid Mechanics, 714:489–504, January 2013.